# Exploring the role of disulfidptosis-related signatures in immune microenvironment, prognosis and therapeutic strategies of cholangiocarcinoma

YUE CHEN[1], JUN WU[1], DANXIA ZHU[1], LU JIANG[1], JIAN WANG[1], DACHUAN ZHANG[2] and WENTING HE[1]

[1]Department of Oncology, The Third Affiliated Hospital of Soochow University, Changzhou, Jiangsu 213003, P.R. China;
[2]Department of Pathology, The Third Affiliated Hospital of Soochow University, Changzhou, Jiangsu 213003, P.R. China

Received August 13, 2025; Accepted November 27, 2025

DOI: 10.3892/or.2026.9042

**Abstract.** Cholangiocarcinoma (CCA) is an aggressive malignancy with poor prognosis and a limited number of treatments is available. Disulfidptosis, a newly identified form of cell death triggered by disulfide bond accumulation during glucose deprivation, may influence cancer progression but its role in CCA is poorly understood. The present study investigated disulfidptosis-related genes (DRGs) and their impact on CCA prognosis and immune modulation. Differential expression analysis of 100 DRGs using RNA sequencing data from The Cancer Genome Atlas and EMBL-EBI identified 74 dysregulated genes in CCA. Unsupervised clustering stratified patients with CCA into two distinct subtypes (Subs): i) SubA; and ii) SubB. A four-gene prognostic signature was developed using least absolute shrinkage and selection operator regression and validated via Kaplan-Meier survival analysis and receiver operating characteristic curves. Immune infiltration and tumor microenvironment were evaluated using Cell-type Identification by Estimating Relative Subsets of RNA Transcripts, Estimation of Stromal and Immune cells in Malignant Tumor tissues using Expression data and single-sample Gene Set Enrichment Analysis. Functional assays, including small interfering RNA knockdown of *CD109* and *EFNB2* in CCA cell lines were used to investigate proliferation, migration, invasion and F-actin staining. Results showed SubB, associated with higher disulfidptosis activity, had worse prognosis, increased immune cell infiltration and elevated immune checkpoint gene expression. The four-gene signature effectively stratified patients into risk groups. Knockdown of *CD109* and *EFNB2* significantly suppressed CCA cell proliferation, migration and invasion while it promoted disulfidptosis under glucose deprivation. The present study established an association between DRGs and CCA prognosis/immune dynamics, provided a robust four-gene prognostic signature, and identified *CD109* and *EFNB2* as potential therapeutic targets, positioning disulfidptosis as a promising focus for precision medicine in CCA.

*Correspondence to:* Dr Dachuan Zhang, Department of Pathology, The Third Affiliated Hospital of Soochow University, 185 Juqian Street, Changzhou, Jiangsu 213003, P.R. China
E-mail: zhangdachuan@suda.edu.cn

Dr Wenting He, Department of Oncology, The Third Affiliated Hospital of Soochow University, 185 Juqian Street, Changzhou, Jiangsu 213003, P.R. China
E-mail: wth311@126.com

*Abbreviations:* CCA, cholangiocarcinoma; EMBL-EBI, European Molecular Biology Laboratory-European Bioinformatics Institute; TCGA, The Cancer Genome Atlas; DRGs, Disulfidptosis-related genes; KM, Kaplan-Meier; GSVA, gene set enrichment analysis; DEGs, differentially expressed genes; ssGSEA, single-sample gene set enrichment analysis; GSEA, gene set enrichment analysis; LASSO, least absolute shrinkage and selection operator; OS, overall survival; ROC, receiver operating characteristic; DCA, clinical decision curves; EFNB2, ephrin-B2; TME, tumor microenvironment; TMB, tumor mutational burden; ADAMTS12, A disintegrin and metalloproteinase with thrombospondin motifs 12; KLK6, Kallikrein-related peptidase 6; RCD, regulated cell death; ESTIMATE, Estimation of Stromal and Immune cells in Malignant Tumor tissues using Expression; CIBERSORT, Cell-type Identification by Estimating Relative Subsets of RNA Transcripts; RT-qPCR, reverse transcription-quantitative PCR; WB, western blot analysis; CCK-8, Cell Counting Kit-8; IF, immunofluorescence; EMT, epithelial-mesenchymal transition

*Key words:* disulfidptosis, cholangiocarcinoma, immune microenvironment, bioinformatics, prognosis signature, CD109, EFNB2

## Introduction

Cholangiocarcinoma (CCA), an aggressive cancer originating from the biliary epithelium, is the 2nd most common primary liver cancer after hepatocellular carcinoma (1-4). Histologically, CCA is typically an adenocarcinoma characterized by dense desmoplastic stroma and a complex tumor microenvironment (TME) enriched with cancer-associated fibroblasts and immunosuppressive cells, which collectively foster tumor progression and resistance to therapy (5,6). Due to the absence of early symptoms and lack of effective screening tools, only 15-30% of patients with CCA are eligible for curative resection at diagnosis (with >65% presenting with unresectable or metastatic disease), and recurrence rates after curative-intent surgery remain high (50-83%) (7-9). The standard first-line chemotherapy regimen, gemcitabine combined with cisplatin,

confers limited benefit. Although targeted therapies against *FGFR2* and *IDH1* mutations have shown promise in subsets of patients, resistance frequently emerges (10). The combination of molecular heterogeneity, immunosuppressive TME and intrinsic chemoresistance results in poor outcomes, with a median survival of only 4-8 months and a 5-year survival rate of <20% (11). Thus, there is an urgent need to identify novel biomarkers and therapeutic targets tailored to the molecular and anatomical diversity of CCA.

Targeting specific molecular pathways and harnessing the mechanisms of regulated cell death (RCD) have emerged as promising strategies for cancer suppression (12-15). Recently, a distinct RCD form termed disulfidptosis has been identified, characterized by cytoskeletal collapse caused by excessive disulfide bonding in actin filaments under glucose-deprived conditions (16,17). In cells overexpressing SLC7A11, continuous cystine uptake depletes NADPH, hindering disulfide bond reduction and promoting toxic protein crosslinking. Notably, disulfidptosis is unresponsive to classical RCD inhibitors and can occur independently of ATP levels. Therapeutic strategies that enhance thiol oxidation or inhibit glucose uptake exacerbate disulfide stress and trigger this cell death pathway (16,17). Emerging studies implicate disulfidptosis in digestive tract malignancies such as gastric and hepatocellular carcinoma, where disulfidptosis-related gene (DRG) expression is associated with immune activity and clinical prognosis (18-26). However, its role in CCA remains unexplored.

Notably, research has highlighted key features of CCA biology that suggest a unique vulnerability to disulfidptosis. First, CCA is dependent on glucose metabolism and undergoes extensive metabolic reprogramming to survive in a nutrient-poor TME, creating a state of chronic metabolic stress (5,27). Second, the aggressive, invasive nature of CCA is dependent on the dynamic reorganization of the actin cytoskeleton, and an abnormal actin network is itself a driver of the malignant phenotype and metastasis (28). Furthermore, the emerging susceptibility of CCA to other forms of redox-dependent cell death such as ferroptosis points towards a reliance on solute carriers such as the cystine-glutamate transporter xCT, which includes SLC7A11, to manage oxidative stress (29). These characteristics, glucose dependency, cytoskeletal vulnerability and active SLC7A11-related pathways, establish a rationale for investigating disulfidptosis, a novel cell death pathway that is directly associated with all three of these biological pillars.

To investigate this unexplored area, DRGs in CCA were systematically evaluated using RNA sequencing data from The Cancer Genome Atlas (TCGA) and European Molecular Biology Laboratory-European Bioinformatics Institute (EMBL-EBI). Differential expression analysis was performed to identify candidate DRGs, then unsupervised clustering was used to define patient subgroups with distinct clinical and molecular characteristics. Building on these findings, a prognostic signature was developed using least absolute shrinkage and selection operator (LASSO) regression and validated through functional assays to elucidate the ways key DRGs regulate disulfidptosis. To the best of our knowledge, the present study revealed the first comprehensive landscape of disulfidptosis in CCA, associating DRG activity to patient survival, immune microenvironment remodeling and therapeutic responsiveness. These findings not only offer a prognostic tool, but also highlight actionable targets, opening new avenues for treating this intractable malignancy. The workflow of the present study is shown in Fig. 1.

## Materials and methods

*Data collection and processing*. To construct and validate the prognostic signature, independent training and validation cohorts were used. The present study conducted a systematic search of public repositories, including the Gene Expression Omnibus (GEO), The Cancer Genome Atlas (TCGA) and ArrayExpress. For the training cohort, the E-MTAB-6389 dataset (https://www.ebi.ac.uk/biostudies/studies/E-MTAB-6389) was selected from the ArrayExpress database (https://www.ebi.ac.uk/arrayexpress/) after a systematic search of public repositories. The dataset was chosen due to its larger sample size (n=75) which provided greater statistical power for the initial model construction. This dataset contains gene expression data from 75 CCA tissues and 31 adjacent normal tissues, generated on the Affymetrix Human Transcriptome Array 2.0 microarray platform (GEO platform accession, GPL17585). The raw data were processed using the robust multi-array average algorithm and subsequently log2-transformed. For external validation, TCGA-CHOL cohort was used, acquired from the Genomic Data Commons portal (https://portal.gdc.cancer.gov/). This cohort consisted of 35 patients with CCA and corresponding overall survival (OS) data. Gene expression was quantified as Fragments Per Kilobase of transcript per Million mapped reads (FPKM) on the Illumina HiSeq 2000 platform (Illumina, Inc.), and the values were log2-transformed [log2(FPKM+1)] for subsequent analyses. Due to incomplete clinical information in the training cohort, survival modeling and mutation profiling were performed exclusively on TCGA dataset. A total of 100 DRGs were identified through a systematic literature review. The selection process began with core mechanistic genes established in foundational studies, and was expanded by incorporating DRGs from recent high-quality bioinformatics and experimental studies that constructed prognostic models or molecular subtypes (molecular subs; distinct tumor subgroups characterized by specific disulfidptosis-related gene expression profiles and clinical outcomes) across malignancies (Table SI) (16-26). All datasets are publicly available and adhere to ethical standards. The harmonized clinicopathological characteristics for subsequent analyses are elaborated in Table I.

*Expression of DRGs and molecular subtyping in CCA*. An integrated analysis of 100 DRGs in CCA was conducted. Expression profiles were extracted from the E-MTAB-6389 dataset, and differential expression was assessed using Wilcoxon rank-sum tests (FDR <0.05). Significant DRGs were visualized using boxplots. Pairwise co-expression relationships were evaluated using Pearson's correlation analysis. All statistical and bioinformatic analyses were performed using R version 4.4.1 (30). Somatic mutation landscapes were analyzed using TCGA data and the 'maftools' package (31) (https://bioconductor.uib.no/packages/release/bioc/html/maftools.html) version 2.18.0, with

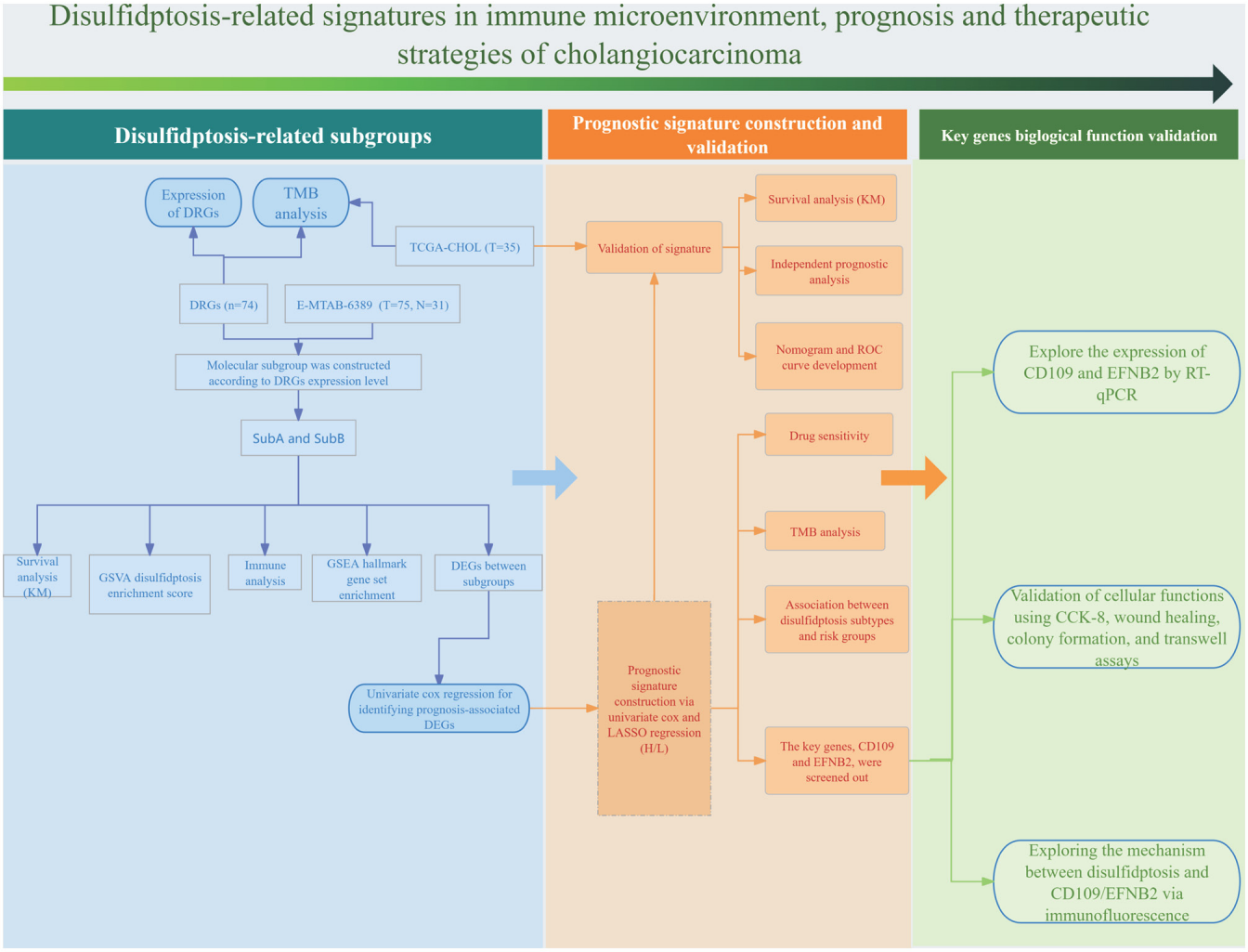


Figure 1. Flow chart for the present study analysis. DRGs (n=74) expression was assessed in the E-MTAB-6389 cohort (T=75, N=31), dividing patients into SubA and SubB based on DRG levels. Molecular subtyping was followed by survival analysis (KM), GSVA enrichment score, immune analysis and GSEA hallmark enrichment. Prognosis-related DEGs were identified and used to build a signature via univariate Cox and LASSO regression, validated in the TCGA-CHOL cohort (T=35) with KM survival, independent prognostic, nomogram, ROC, drug sensitivity and TMB analyses. Disulfidptosis subtypes and risk groups were explored, highlighting CD109 and EFNB2, validated by RT-qPCR and functional assays. The disulfidptosis-CD109/EFNB2 mechanism was investigated via immunofluorescence. DRGs, disulfidptosis-related genes; TCGA, The Cancer Genome Atlas; GSVA, gene set variation analysis; GSEA, Gene Set Enrichment Analysis; LASSO, least absolute shrinkage and selection operator; KM, Kaplan-Meier; ROC, receiver operating characteristic; TMB, tumor mutational burden; RT-qPCR, real-time quantitative polymerase chain reaction; CCK-8, Cell Counting Kit-8; TCGA-CHOL, cholangiocarcinoma cohort from The Cancer Genome Atlas database; T, tumor; N, normal.

alterations depicted in waterfall plots. To identify disulfidptosis-driven molecular Subs, unsupervised consensus clustering was performed on tumor samples using the 'ConsensusClusterPlus' package (32) (https://bioconductor.org/packages/release/bioc/html/ConsensusClusterPlus.html) version 1.54.0.

*Prognostic, immune microenvironment and mechanistic profiling of disulfidptosis-related molecular Subs in CCA*. To investigate the prognostic and biological significance of disulfidptosis-related molecular Subs in CCA, survival analysis was performed to compare OS across Subs. Enrichment scores for disulfidptosis pathways were computed by integrating gene sets with CCA expression matrices using the 'GSVA' R package, with Sub-specific differences assessed via Wilcoxon tests. For immune microenvironment analysis, three complementary approaches were used. Stromal and immune cell infiltration scores were quantified using the Estimation of Stromal and Immune cells in Malignant Tumor tissues using Expression data (ESTIMATE) algorithm with the 'estimate' R package. Proportions of 22 immune cell types were estimated through Cell-type Identification by Estimating Relative Subsets of RNA Transcripts (CIBERSORT) deconvolution using the 'CIBERSORT' R package. Immune cell-specific enrichment scores were derived via single-sample (ss) Gene Set Enrichment Analysis (GSEA) with the 'GSVA' R package. Subtype differences were evaluated using Wilcoxon tests. Expression profiles of immune checkpoint and human leukocyte antigen (HLA) family genes were compared across Subs. Molecular pathway characterization was performed using GSEA.

*Identification of DRGs, and construction and validation of the prognostic signature in CCA*. Utilizing the 'limma' package in R, P-values and log2FC were calculated for

Table I. Clinicopathological characteristics of patients with cholangiocarcinoma in The Cancer Genome Atlas.

| Clinicopathological characteristics | TCGA cohort (N=35) |
|---|---|
| Age (years), no. (%) | |
| ≤65 | 17 (48.6%) |
| >65 | 18 (51.4%) |
| Gender, no. (%) | |
| Female | 19 (54.3%) |
| Male | 16 (45.7%) |
| Stage, no. (%) | |
| I | 18 (51.4%) |
| II | 9 (25.7%) |
| III | 1 (2.9%) |
| IV | 7 (20%) |
| T, no. (%) | |
| 0 | 0 (0.0%) |
| 1 | 18 (51.4%) |
| 2 | 6 (17.1%) |
| 2a | 2 (5.7%) |
| 2b | 4 (11.5%) |
| 3 | 5 (14.3%) |
| 4 | 0 (0.0%) |
| N, no. (%) | |
| N0 | 25 (71.4%) |
| N1 | 5 (14.3%) |
| NX | 5 (14.3%) |
| M, no. (%) | |
| M0 | 27 (77.1%) |
| M1 | 5 (14.3%) |
| MX | 3 (8.6%) |
| Survival status, no. (%) | |
| Alive | 17 (48.6%) |
| Dead | 18 (51.4%) |
| Overall survival time, days | |
| Mean ± SD | 742.54±548.58 |
| Median | 640 |

each gene, applying multiple testing correction to obtain adjusted P-values (adj.P.Value). Genes with adj.P.Value <0.05 and |log2FC|>0.585 were classified as differentially expressed and disulfidptosis related. To identify prognostic Sub-specific genes, univariate Cox regression analysis was conducted using gene expression and survival data from CCA samples. Genes with P<0.01 were deemed significant. A prognostic model was then constructed using LASSO regression analysis using the 'lars' package, incorporating 10-fold cross-validation for gene selection. The risk score formula, RiskScore=β1X1 + β2X2 + ... + βnXn, was employed, where β signifies LASSO regression coefficients and X represents gene expression levels. Risk scores were calculated for each sample in both the EMBL-EBI training set and TCGA validation cohort, with patients stratified into high (H)-risk and low (L)-risk groups based on an optimal risk score cut-off. Kaplan-Meier assessed the association between risk groups and survival outcomes. Univariate and multivariate Cox regression analyses determined whether the model functioned as an independent prognostic factor for CCA. Significant clinical features were incorporated into a nomogram constructed with the 'rms' R package. Calibration curves assessed model consistency, while receiver operating characteristic (ROC) curves and clinical decision curves evaluated the nomogram's predictive accuracy and practical utility.

*Drug sensitivity analysis of risk groups*. Drug sensitivity was analyzed between H- and L-risk groups by employing predicted $IC_{50}$ values sourced from the Genomics of Drug Sensitivity in Cancer (https://www.cancerrxgene.org/). Utilizing the 'pRRophetic' R package, $IC_{50}$ values were computed. Significant disparities in drug sensitivity among the risk subgroups were uncovered using Wilcoxon rank-sum tests, highlighting therapeutic diversity.

*Mutational landscape stratification by risk groups*. For the analysis of somatic variant profiles from TCGA cohorts, the 'maftools' package was employed to investigate oncogenic landscapes across risk subgroups. The varying mutation frequencies among the top 20 driver genes were visualized using 'oncoplots'. Additionally, the tumor mutational burden (TMB) was quantified and evaluated using the Wilcoxon rank-sum test.

*Association between disulfidptosis Subs and risk groups*. To explore the relationship between disulfidptosis Subs and risk groups, the R 'ggalluvial' package was used to generate Sankey diagrams. These diagrams visually represented the distribution of samples across disulfidptosis Subs and H-/L-risk groups, revealing the associations between these classifications.

*Cell culture*. HuCCT1 cells (Procell Life Science & Technology Co., Ltd.), primary human intrahepatic bile duct epithelial cells (HiBEpiCs; passage 2; cat. no. CP-H042; Pricella Biotechnology), RBE cells (The Cell Bank of Type Culture Collection of The Chinese Academy of Sciences) and HuH-28 cells (cat. no. ZQ1030; Zhong Qiao Xin Zhou Biotechnology Co., Ltd.) were cultured in RPMI-1640 medium (HyClone; Cytiva) supplemented with 10% fetal bovine serum (FBS; Gibco; Thermo Fisher Scientific, Inc.) at 37˚C in a humidified 5% $CO_2$ incubator (Heal Force Bio-Meditech Holdings, Ltd.). All cell handling procedures were performed in a biological safety cabinet (BHC-1300IIA2; Suzhou Antai Air Technology Co., Ltd.). For thawing, cells were rapidly thawed in a 37˚C water bath (HWS-12; Shanghai Yiheng Scientific Instrument Co., Ltd.) and gently agitated. After centrifugation (200 x gp; 5 min; room temperature), cells were resuspended in culture medium, seeded into dishes and incubated at 37˚C with 5% $CO_2$. When cells achieved 80-90% confluency, they were trypsinized, centrifuged (200 x g; 5 min; room temperature) and re-seeded. For cryopreservation, $5x10^6$ cells/ml were resuspended in Cell Freezing Medium (cat. no. C0210; Beyotime Biotechnology), aliquoted into cryovials and frozen at -80˚C before storage in liquid nitrogen.

Table II. siRNA sequences about CD109, EFNB2 and si-NC.

| siRNA | Sense, 5'-3' | Antisense, 5'-3' |
|---|---|---|
| si-NC | UUCUCCGAACGUGUCACGU (dT dT) | ACGUGACACGUUCGGAGAA (dT dT) |
| CD109-siRNA1 | AUCAAACCUCACUGUCUCU (dT dT) | AGAGACAGUGAGGUUUGAU (dT dT) |
| CD109-siRNA2 | ACACUUACUCUUCCAUCAC (dT dT) | GUGAUGGAAGAGUAAGUGU (dT dT) |
| CD109-siRNA3 | ACAAGCCAAAGCAAGAAGU (dT dT) | ACUUCUUGCUUUGGCUUGU (dT dT) |
| EFNB2-siRNA1 | ACCUGGACAAGGACUGGUA (dT dT) | UACCAGUCCUUGUCCAGGU (dT dT) |
| EFNB2-siRNA2 | GUUGGCCAGUAUGAAUAUU (dT dT) | AAUAUUCAUACUGGCCAAC (dT dT) |
| EFNB2-siRNA3 | GUGCCAAACCAGACCAAGA (dT dT) | UCUUGGUCUGGUUUGGCAC (dT dT) |

Si, small interfering; NC, negative control.

*Small interfering (si)RNA transfection*. siRNA transfection was performed to knock down *CD109* and *EFNB2* expression in HuCCT1 and RBE cells. The specific siRNA sequences (listed in Table II) were synthesized by Sangon Biotech Co., Ltd. A total of $5x10^5$ cells/ml were seeded in 2 ml culture medium in a 6-well plate and incubated for 24 h at 37˚C in a 5% $CO_2$ incubator. siRNAs [negative control (NC) siRNA, CD109 siRNA and EFNB2 siRNA] were diluted to 100 pmol/$\mu$l. For transfection, 1 $\mu$l siRNA was mixed with 150 $\mu$l Opti-MEM (Gibco; Thermo Fisher Scientific, Inc.) and incubated for 5 min at room temperature. Similarly, 5 $\mu$l Lipofectamine™ RNAiMAX (cat. no. 13778150; Thermo Fisher Scientific, Inc.) was mixed with 150 $\mu$l Opti-MEM. After 20 min of incubation at room temperature, the transfection complex was added dropwise to the cells. After 6 h at 37˚C, the medium was replaced with DMEM (cat. no. 11965-118; Gibco; Thermo Fisher Scientific Inc.) containing 10% FBS, and cells were cultured for further analysis. Transfection efficiency and plasmid construction were validated using quantitative PCR (qPCR) and western blotting (WB) 24 h post-transfection.

*Reverse transcription (RT)-qPCR*. Total RNA was extracted from normal intrahepatic biliary epithelial cells (HIBEpiC) and CCA cell lines (HuCCT1, RBE, and HuH-28) using 1 ml TRIzol® (Thermo Fisher Scientific, Inc.), followed by chloroform separation, isopropanol precipitation and ethanol washing. RNA concentration and purity were assessed using a NanoDrop 2000. cDNA was synthesized from 1 $\mu$g RNA using Reverse Transcriptase (Thermo Fisher Scientific, Inc.) with Oligo-dT. The reaction was incubated at 70˚C for 5 min, 37˚C for 5 min, 42˚C for 60 min and 70˚C for 5 min. qPCR was performed to a 10 $\mu$l reaction containing 4 $\mu$l diluted cDNA, 5 $\mu$l BeyoFast™ SYBR Green qPCR Mix (2X) (cat. no. D7260; Beyotime Biotechnology), 0.4 $\mu$l forward and reverse primer (10 $\mu$M) and 0.6 $\mu$l water on a CFX96 system. The thermocycling conditions for qPCR were: 95˚C for 5 min, 40 cycles of 95˚C for 10 sec and 60˚C for 20 sec, followed by a melting step and cooling at 40˚C for 30 sec. Data were analyzed using the $2^{-\Delta\Delta Cq}$ method (33) with *GAPDH* as the reference gene. Primer sequences are shown in Table III.

*WB*. Total protein was collected from HuCCT1 and RBE cells using RIPA lysis buffer (Beyotime Biotechnology) supplemented with protease and phosphatase inhibitors. The lysate was collected by centrifugation at 14,000 x g for 15 min at 4˚C, and protein concentration was measured using a BCA Protein Assay Kit (cat. no. P0012; Beyotime Biotechnology). Samples were mixed with 4X Sample Buffer (Beyotime Biotechnology) containing 100 mM dithiothreitol, denatured at 95˚C for 5 min and separated on 4-20% Bis-Tris gels (cat. no. M00657; GenScript). Proteins were transferred to PVDF membranes which were then blocked with 5% non-fat milk in TBS-Tween [TBST; Tris-buffered saline containing 0.1% (V/V) Tween 20] for 2 h at room temperature. The membranes were subsequently incubated with primary antibodies diluted in TBST containing 5% bovine serum albumin (Sigma-Aldrich; Merck KGaA). The specific primary antibodies used were: CD109 (1:1,000; cat. no. A23787; ABclonal Biotech Co., Ltd.) and Ephrin B2 Polyclonal antibody (1:1,500; cat. no. 26533-1-AP; Proteintech Group, Inc.). The incubation was performed overnight (12-16 h) at 4˚C on a shaker. Following primary antibody incubation, membranes were washed three times with TBST (10 min each) and incubated with HRP-linked secondary antibody (1:6,000; cat. no. 7074; Cell Signaling Technology Inc.) for 1 h at room temperature for detection. For the loading control, membranes were probed separately using GAPDH (D16H11) Rabbit mAb (HRP Conjugate) (cat. no. 8884; Cell Signaling Technology Inc.), which was detected directly. Chemiluminescent signals were captured with a Tanon-4600 imaging system and analyzed using Quantity One (version 4.6.6; Bio-Rad Laboratories, Inc.).

*Cell Counting Kit-8 (CCK-8) assay*. A total of $2x10^4$ cells/ml were seeded in 100 $\mu$l DMEM with 10% FBS in 96-well plates and incubated for 24 h at 37˚C with 5% $CO_2$. At 0, 24, 48 and 72 h, 10 $\mu$l CCK-8 solution (Beyotime Biotechnology) was added to each well, avoiding bubbles. Plates were incubated for 1 h at 37˚C, and absorbance was measured at 450 nm using a microplate reader.

*Cell cloning assay*. Cells were serially diluted and seeded at 100 cells per 60-mm dish. Dishes were gently rotated for even distribution and incubated at 37˚C with 5% $CO_2$ for 2-3 weeks. When visible clones appeared, the medium was removed and cells were washed twice with 1X PBS, fixed with 4% paraformaldehyde for 15 min at room temperature and stained with 0.1% crystal violet for 10-30 min at room temperature. After washing and air drying, clones were imaged using a

Table III. Reverse transcription-quantitative PCR primer sequences.

| Gene | Sense, 5'-3' | Antisense, 5'-3' |
|---|---|---|
| CD109 | AAGCCAGTGAAAGGAGACGTA | CCAGGGGAAGATAGATCCAGG |
| EFNB2 | TATGCAGAACTGCGATTTCCAA | TGGGTATAGTACCAGTCCTTGTC |
| GAPDH | GGAGCGAGATCCCTCCAAAAT | GGCTGTTGTCATACTTCTCATGG |

light microscope and imaging system (Olympus Corporation) and quantified with ImageJ software (version 1.54; National Institutes of Health).

*Wound healing assay*. A total of $5x10^5$ HuCCT1 and RBE tumor cells/well were seeded in 6-well plates and cultured for 16-24 h at 37˚C until 90% confluence. A 10-$\mu$l pipette tip was used to create 3-5 linear scratches per well. Cells were washed three times with PBS to remove debris and cultured in serum-free DMEM for 24 h at 37˚C. Wound closure was imaged at 0 and 24 h using a light microscope (Nikon Corporation) and analyzed using ImageJ software (version 1.54; National Institutes of Health).

*Transwell assay*. Tumor cell migration and invasion were assessed using 24-well Transwell inserts with an 8-$\mu$m pore size polycarbonate membrane. For the migration assay, cells were trypsinized using 0.25% Trypsin-EDTA, centrifuged at 300 x g for 5 min at room temperature, washed twice with PBS and resuspended in serum-free RPMI-1640 medium with 1% FBS to a concentration of $5x10^5$ cells/ml. Subsequently, 200 $\mu$l of the cell suspension ($1x10^5$ cells) was seeded into the upper chamber. For the invasion assay, Transwell inserts were pre-coated with Matrigel Matrix and solidified for 1 h at 37˚C before seeding cells. RPMI-1640 medium containing 20% FBS was added to the lower chamber as a chemoattractant. The plates were incubated for 24 h at 37˚C in a humidified atmosphere containing 5% $CO_2$. Non-migrated cells on the upper surface were removed using cotton swabs. Migrated or invaded cells on the lower surface were fixed with 4% paraformaldehyde for 30 min at room temperature and stained with 0.1% crystal violet solution for 20 min at room temperature. The inserts were washed with PBS, and the stained cells were imaged and counted using ImageJ software (version 1.54; National Institutes of Health) for quantitative analysis.

*F-actin immunofluorescence staining*. A total of $2x10^4$ cells/ml were added in 500 $\mu$l medium in 6-well plates (Corning, Inc.) and cultured in DMEM (cat. no. 11965-118; Gibco; Thermo Fisher Scientific, Inc.) for 24 h at 37˚C with 5% $CO_2$ until reaching 50% confluence. To investigate the role of EFNB2 and CD109 in disulfidptosis, the medium was replaced with glucose-free DMEM (cat. no. 11966-025; Gibco; Thermo Fisher Scientific, Inc.) for glucose deprivation. Cells were then treated with the GLUT1 inhibitor BAY-876 (10 $\mu$M; cat. no. HY-100017, MedChemExpress) and/or the reducing agent, Tris-(2-carboxyethyl)-phosphine hydrochloride (TCEP; 20 mM; cat. no. A600974; Sangon Biotech Co., Ltd.) for 6 h at 37˚C. Following treatment, cells were washed twice with pre-warmed 1X PBS (pH 7.4; Sangon Biotech Co., Ltd.). Cells were fixed with 4% paraformaldehyde (Shanghai Lingfeng Chemical Reagent Co., Ltd.) in PBS for 10 min at room temperature, followed by three PBS washes. Permeabilization was performed with 0.5% Triton X-100 (Bio-Rad Laboratories, Inc.) in PBS for 5 min at room temperature, followed by PBS washes. Cells were then incubated with Alexa Fluor™ 594 Phalloidin (1:400 dilution in 1% BSA/PBS; cat. no. A12381, Thermo Fisher Scientific Inc.) for 30 min in a, humidified chamber in the dark. After washing, cells were counterstained with DAPI (100 nM; cat. no. HY-D0814, MedChemExpress) for 30 sec at room temperature. Coverslips were mounted on slides with AntiFade Mounting Medium (cat. no. HY-K1042; MedChemExpress) and sealed. Fluorescence was observed using a ZEISS LSM800 confocal microscope (ZEISS).

*Statistical analysis*. Statistical analysis was conducted using R (version 4.4.1; The R Foundation for Statistical Computing), SPSS (version 26.0; IBM Corp.) and GraphPad Prism (version 10.0; Dotmatics). Intergroup comparisons were carried out using the Wilcoxon rank-sum test, while chi-square tests assessed association between subgroups and clinicopathological features. Survival curves were plotted using the Kaplan-Meier method. Prognostic factors for CCA were identified via LASSO regression, followed by univariate and multivariate Cox regression to calculate hazard ratios (HRs) and 95% confidence intervals (CIs). $P<0.05$ was considered to indicate a statistically significant difference with FDR <0.05. Significance levels are denoted as $^{*}P<0.05$, $^{**}P<0.01$ and $^{***}P<0.001$. All experiments were performed in triplicate.

## Results

*Development of disulfidptosis-regulated clusters and their characteristics in CCA*. Differential expression analysis of 100 DRGs in CCA vs. adjacent normal tissues identified 74 DRGs (|log2FC|>1; FDR <0.05) using Wilcoxon rank-sum tests (Table SII). The top 20 DRGs are shown in Fig. 2A and a correlation heatmap of all 74 DRGs is shown in Fig. 2B. Co-expression analysis of the top 20 DRGs revealed significant intergenic correlations (Fig. 2C). Somatic mutation analysis via TCGA data detected mutations in nine DRGs (Fig. 2D). Unsupervised consensus clustering (K=2; range, 2-10; Fig. 2E) classified 75 samples into SubA (n=34) and SubB (n=41) Subs (Fig. 2F; Table SIII). Sub stability was confirmed using cumulative distribution function curve analysis (Fig. 2G). Kaplan-Meier analysis indicated shorter OS for SubB (P=0.038; Fig. 2H). GSVA revealed elevated disulfidptosis pathway activity in SubB (P=0.005; Fig. 2I; Table SIV).

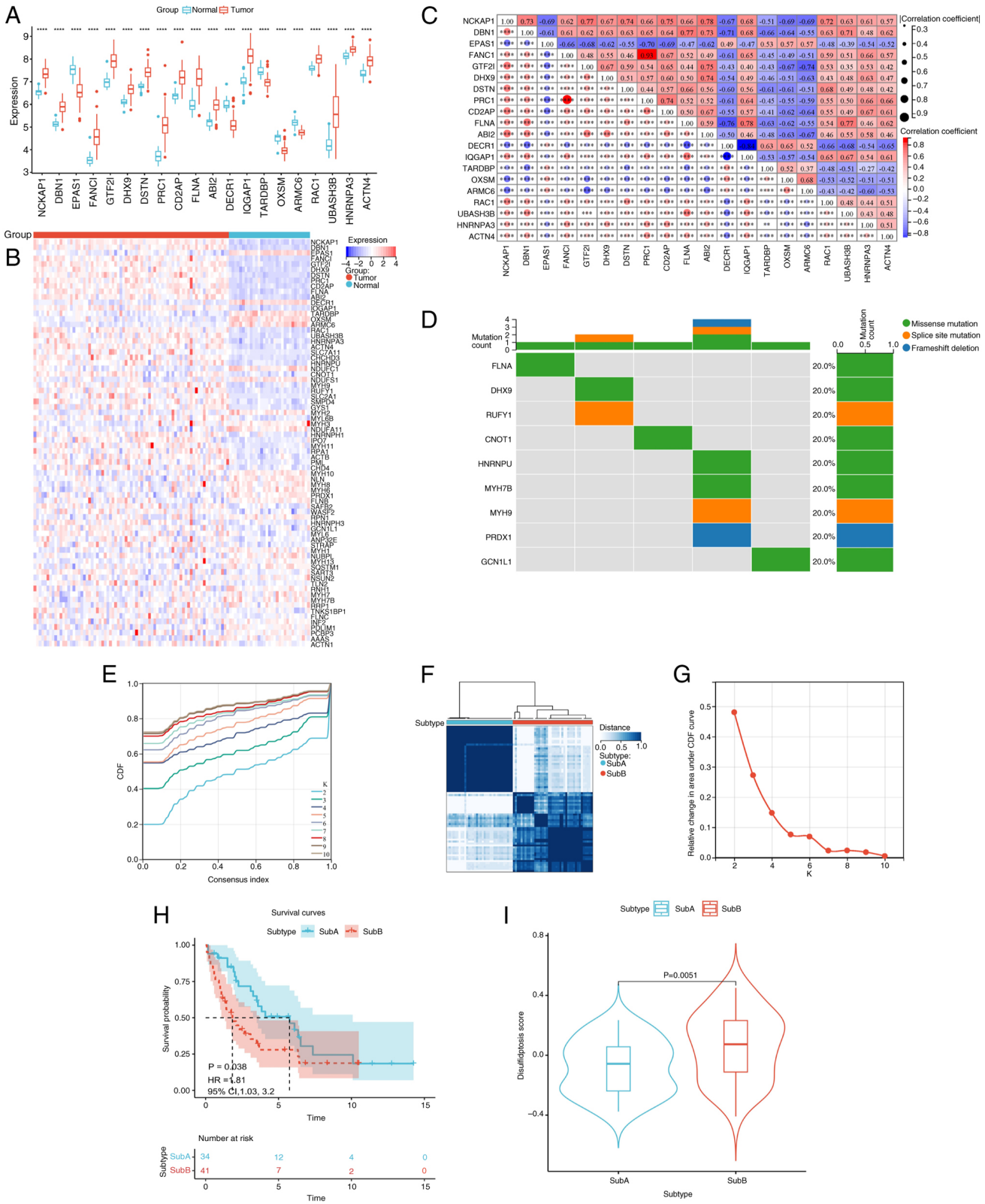


Figure 2. Disulfidptosis-regulated clusters and characteristics in cholangiocarcinoma. (A) Box plots of the top 20 differentially expressed DRGs in cholangiocarcinoma vs. normal samples; (B) heatmap of 74 DRGs in cholangiocarcinoma; (C) correlation matrix heatmap of the top 20 DRGs; (D) waterfall plot of mutations in 74 DRGs; (E) CDF curves for consensus clustering (k=2-10); (F) consensus matrix heatmap at k=2; (G) relative change in CDF Δ area for k values; (H) Kaplan-Meier survival curves for two molecular subtypes (P=0.038; HR=1.81; 95% CI, 1.03-3.2); (I) Violin plots of pathway enrichment score differences between subtypes. ***P<0.001, ****P<0.0001. DRGs, disulfidptosis-related genes; CDF, cumulative distribution function; MutCount, mutation count.

*Immune landscape and checkpoint gene expression profiles in disulfidptosis Subs of CCA*. To investigate the relationship between disulfidptosis Subs and the immune microenvironment in CCA, the CIBERSORT algorithm was applied to evaluate infiltration of 22 immune cell types. Comparative analysis (P<0.05) revealed significantly lower monocyte levels in SubB

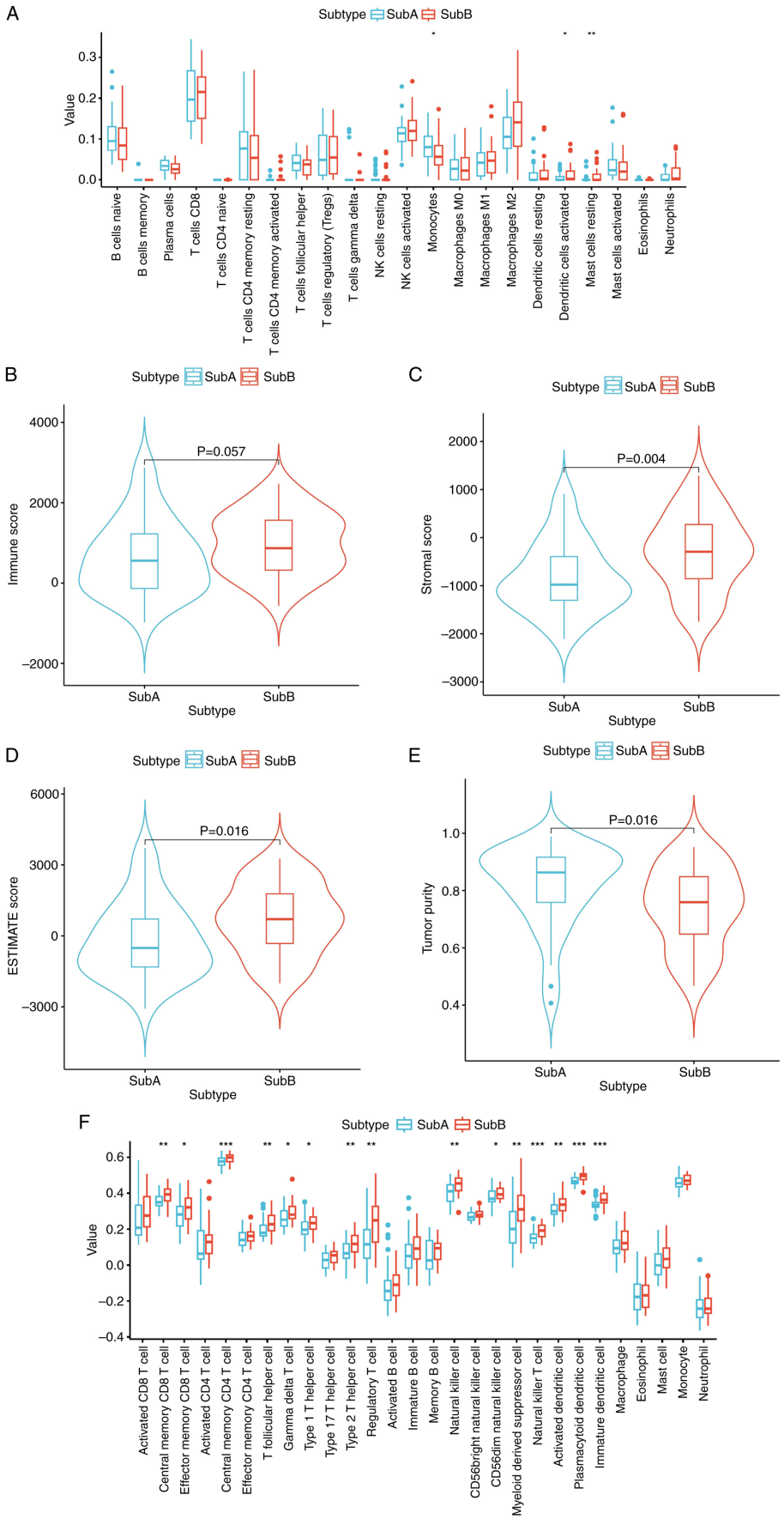


Figure 3. Disulfidptosis subtype-associated immune infiltration in cholangiocarcinoma. (A) Box plots depicting significant differences in immune cell types between subtypes analyzed by CIBERSORT; (B) violin plots comparing immune scores between subtypes; (C) violin plots comparing stromal scores between subtypes; (D) violin plots comparing microenvironment scores between subtypes; (E) violin plots comparing tumor purity between subtypes; (F) box plots showing significant differences in immune cell types between subtypes analyzed by ssGSEA ($^{*}$P<0.05; $^{**}$P<0.01; $^{***}$P<0.001; SubA: blue; SubB: red). NK, natural killer.

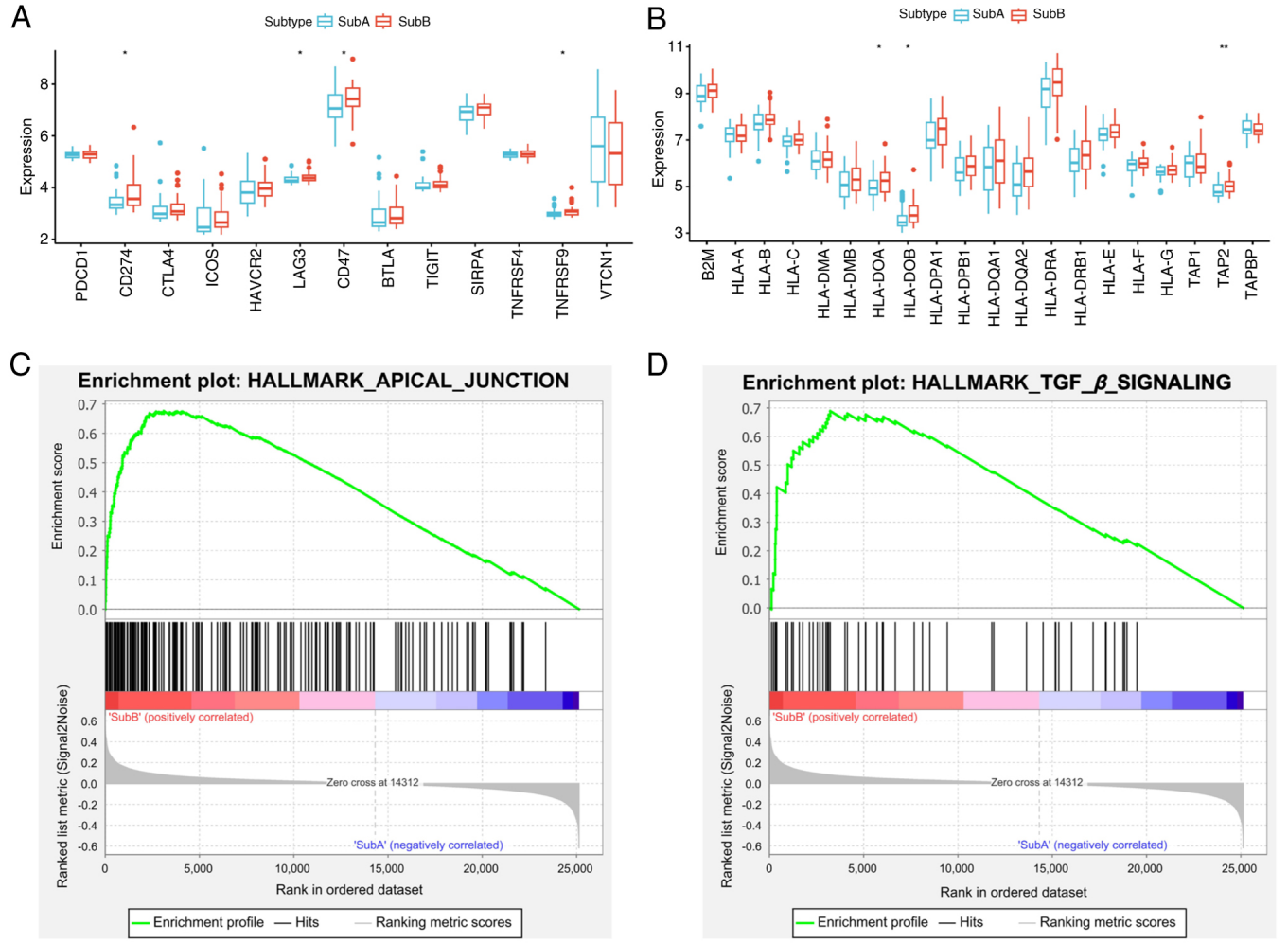


Figure 4. Immune Checkpoint, HLA gene expression and pathway enrichment in disulfidptosis subtypes of cholangiocarcinoma. (A) box plots depicting significant differences in immune checkpoint gene expression between subtypes; (B) box plots showing significant differences in HLA family gene expression between subtypes; (C) GSEA hallmark pathway analysis: APICAL-JUNCTION; (D) GSEA hallmark pathway analysis: TGF-β-SIGNALING. (SubA: blue; SubB: red; $^{*}$P<0.05, $^{**}$P<0.01).

compared with SubA, with an increased number of activated dendritic and resting mast cells in SubB (Fig. 3A). ESTIMATE analysis indicated higher stromal and ESTIMATE scores in SubB (P<0.05), while SubA exhibited greater tumor purity (Fig. 3B-E). Immune scores trended higher in SubB. ssGSEA analysis revealed significantly enhanced effector immune cell activity in SubB, including $CD8^+$ T cells, $CD4^+$ T cells and natural killer cells (P<0.05), indicating robust antitumor immunity (Fig. 3F). By contrast, SubA exhibited elevated levels of γδ T cells and dendritic cells, associated with adaptive immunity and antigen presentation. Immune checkpoint genes (*PD-L1*, *LAG3*, *CD47* and *TNFRSF9*) and HLA antigen presentation genes (*HLA-DOA*, *HLA-DOB* and *TAP2*) were significantly upregulated in SubB (P<0.05; Fig. 4A and B). GSEA analysis of the E-MTAB-6389 dataset revealed SubB enrichment in APICAL_JUNCTION and TGF_β_SIGNALING pathways (Fig. 4C and D; FDR <0.05), suggesting roles in immune evasion and structural remodeling.

*Identifying DRGs, construction and validation of the disulfidptosis-related predictive signature in CCA*. Differentially expressed gene (DEG) analysis between the DRG subgroups identified 190 upregulated genes and 173 downregulated genes (Fig. 5A; Table SV). Univariate Cox regression analysis of the 363 DEGs revealed seven prognosis-related genes (*ADAMTS12*, *SLC2A1*, *CD109*, *CALB2*, *EFNB2*, *KLK6* and *KRT6A*) with P<0.01 and HRs ranging from 1.5 (95% CI, 1.1-1.9) to 2.2 (95% CI, 1.5-3.4; Fig. 5B). LASSO regression selected a four-gene prognostic signature (*EFNB2*, *CD109*, *KLK6* and *ADAMTS12*) with positive coefficients (Fig. 5C and D; Table SVI). The risk score was calculated as follows: RiskScore=0.3589 x Exp (*EFNB2*) + 0.2604 x Exp (*CD109*) +0.2382 x Exp (*ADAMTS12*) + 0.1120 x Exp (*KLK6*).

Using optimal cut-offs (EMBL-EBI; 4.595; TCGA, 1.608), patients with CCA were classified into H- and L-risk groups. Kaplan-Meier analysis revealed significant survival differences in both the EMBL-EBI (P=0.0001; HR, 5.95; 95% CI, 3.03-11.68) and TCGA (P=0.0035; HR, 4.61; 95% CI, 1.51-14.06) datasets (Fig. 5E and F). Heatmaps showed increased expression of the signature genes in H-risk patients, consistent with positive coefficients (Fig. 5G and H). Time-dependent ROC analysis demonstrated area under the curves (AUCs) of 0.680, 0.800 and 0.800 (EMBL-EBI) and 0.660, 0.640 and 0.680 (TCGA; Fig. 5I and J) at 1, 2

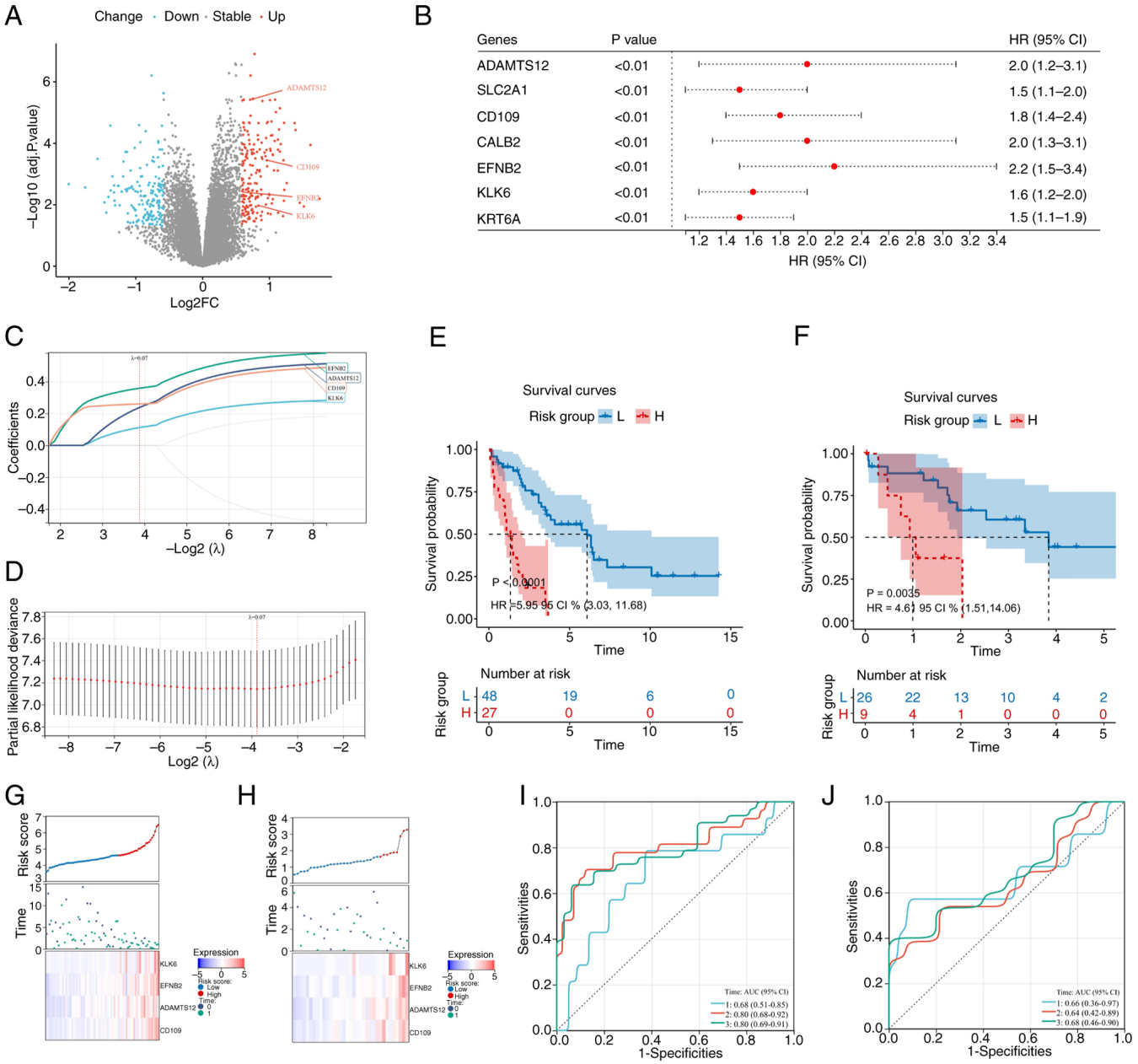


Figure 5. Prognostic gene signature and risk score analysis in cholangiocarcinoma. (A) Volcano plot of differentially expressed genes (blue, downregulated; red, upregulated); (B) Univariate Cox regression forest plot of seven prognostic genes; (C) LASSO coefficient distribution profile; (D) likelihood deviance for LASSO coefficients, with vertical dashed lines indicating λ. min (left) and λ.1se (right); (E) Kaplan-Meier survival curves for patients stratified by the 4-gene signature in the training cohort (Risk group; P<0.0001; HR=5.95; 95% CI 3.03-11.68); (F) Kaplan-Meier survival curves for patients stratified by the 4-gene signature in the validation cohort; (G) training cohort: Risk score distribution (top), survival status (middle) and gene expression heatmap (bottom); (H) validation cohort: Risk score distribution (top), survival status (middle) and gene expression heatmap (bottom); (I) time-dependent ROC curves (1-, 2-, 3-year) in the training cohort; (J) time-dependent ROC curves (1-, 2-, 3-year) in the validation cohort. LASSO, least absolute shrinkage and selection operator; HR, hazard ratio; AUC, area under the curve.

and 3 years, respectively. Univariate and multivariate Cox regression confirmed that the risk score was an independent prognostic factor (P=0.024; HR, 3.353; 95% CI, 1.169-9.616) and multivariate analysis, including age (P=0.023; HR, 1.134; 95% CI, 1.018-1.263) and cancer status (P=0.031; HR, 12.351; 95% CI, 1.258-121.257), further validated its independence (Fig. 6A and B; Table SVII). A nomogram integrating the risk score, age and cancer status achieved AUCs of 0.670, 0.770 and 0.750 for 1-, 2- and 3-year predictions (Fig. 6C and D; Table SVIII). Calibration curves indicated strong agreement between predicted and observed outcomes (Fig. 6E). Decision curve analysis for the 1-, 2- and 3-year outcomes showed that the risk score model provided superior net benefit over age or cancer status alone, especially at medium-to-high thresholds, confirming its clinical utility in risk stratification and treatment decision-making for CCA (Fig. 6F-H).

To elucidate the biological underpinnings of this signature, the genes with the strongest contribution to the risk score were prioritized for functional validation. Given that *EFNB2* and *CD109* possessed the two highest risk coefficients in the LASSO model, they were selected for subsequent *in vitro* experiments.

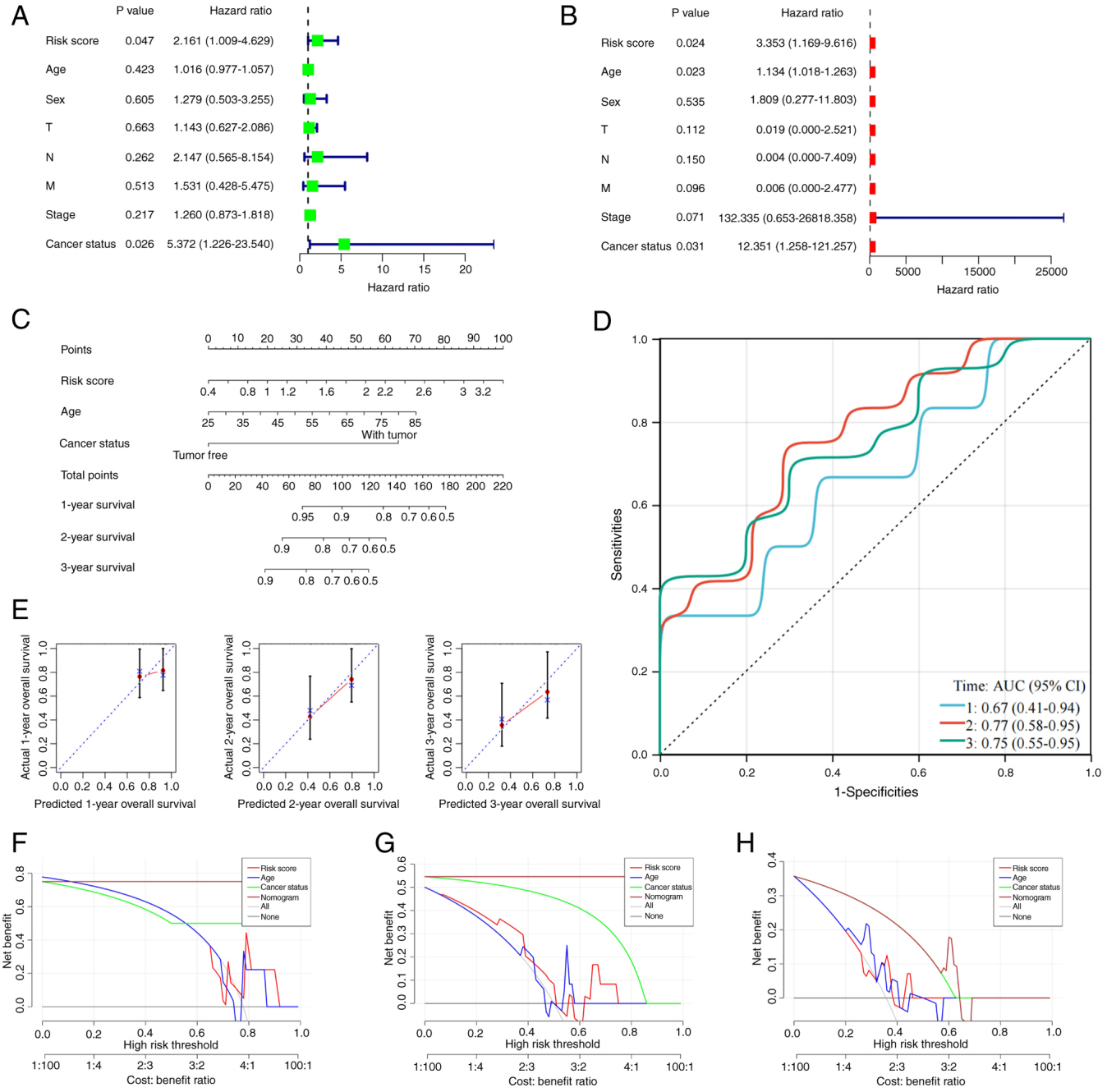


Figure 6. Prognostic model and clinical evaluation in cholangiocarcinoma. (A) Univariate Cox regression analysis of independent prognostic factors; (B) Multivariate Cox regression analysis of independent prognostic factors; (C) Prognostic nomogram integrating independent factors; (D) Time-dependent ROC curves for 1-, 2- and 3-year survival predictions; (E) Calibration curves for 1-, 2- and 3-year survival probabilities; (F) Clinical decision curve analysis DCA for 1-year survival outcomes; (G) DCA for 2-year survival outcomes; (H) DCA for 3-year survival outcomes. DCA, decision curve analysis; AUC, area under the curve.

*Integrated profiling of drug sensitivity, TMB and molecular Subs in the prognostic risk model*. Chemotherapeutic drug sensitivity analysis demonstrated that eight antineoplastic agents, PLX-4720, WZ-1-84, refametinib, PHA-665752, parthenolide, FTI-277, docetaxel and BI2536, exhibited significantly lower $IC_{50}$ values in the H-risk group compared with those in the L-risk group, suggesting heightened chemosensitivity in H-risk patients with CCA. However, no significant difference in efficacy was observed between risk groups for the standard first-line regimen, gemcitabine plus cisplatin ($P<0.05$; Fig. 7A; Table SIX). Mutation analysis identified *PBRM1* as the most frequently altered gene among the top 20 mutated genes (Fig. 7B). TMB analysis using TCGA-CHOL data showed similar distributions across risk groups, with no significant differences in TMB values (Fig. 7C and D). Sankey diagram analysis revealed a predominant clustering of H-risk cases within the SubB disulfidptosis Sub (Fig. 7E), consistent with the association of the Sub with worse clinical outcomes.

*Establishment of CD109 and EFNB2 knockdown CCA cell model*. RT-qPCR was performed to assess mRNA expression of *CD109* and *EFNB2* in three CCA cell lines (HuCCT1, RBE

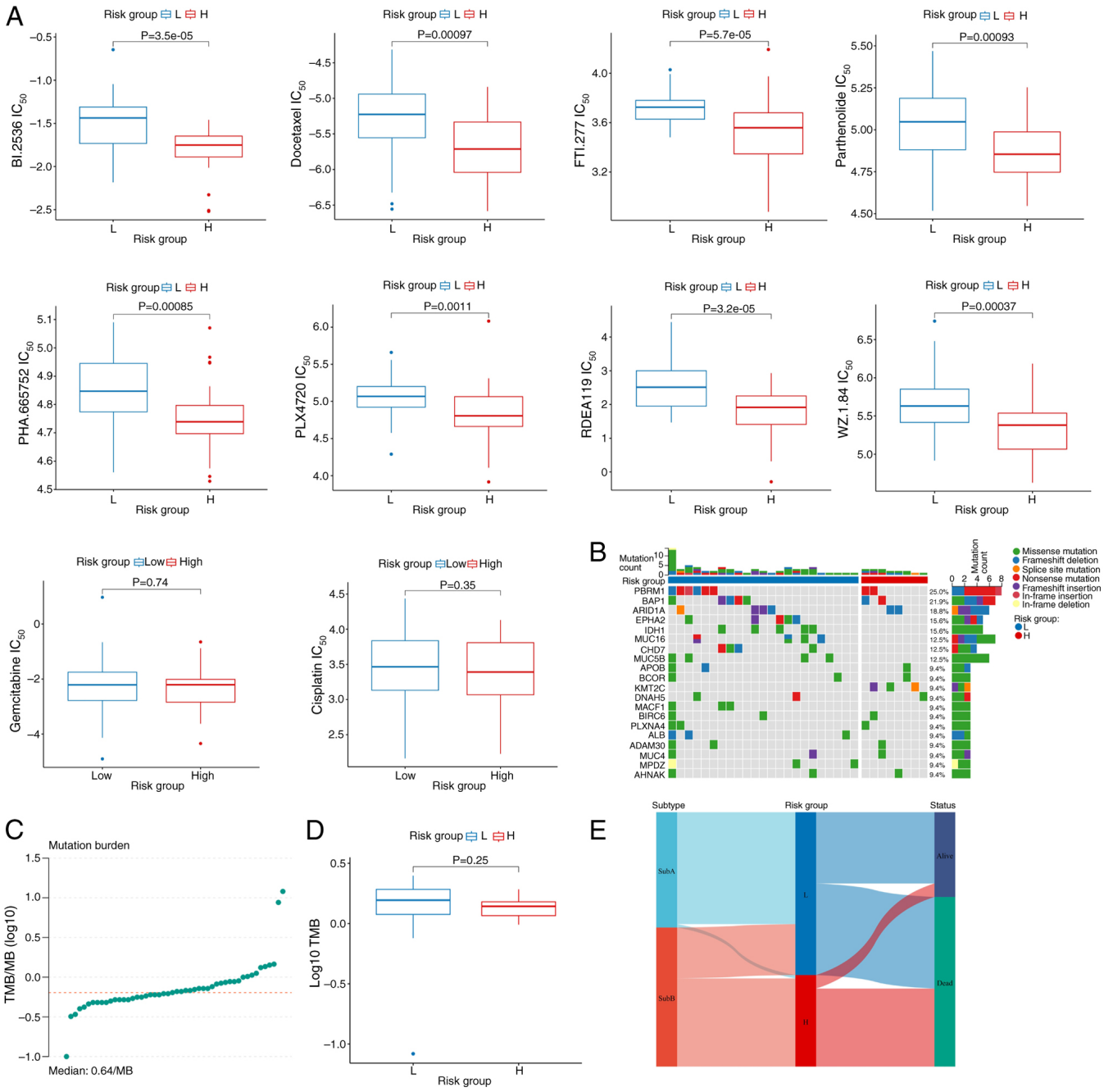


Figure 7. Chemotherapeutic response and genomic characteristics in cholangiocarcinoma. (A) Comparative analysis of $IC_{50}$ levels for 10 chemotherapeutic agents across risk subgroups; (B) waterfall plot of the 20 most frequently mutated genes in cholangiocarcinoma samples; (C) TMB distribution across TCGA-CHOL samples; (D) Box plots comparing TMB between high-risk and low-risk subgroups; (E) Sankey diagram mapping disulfidptosis subtypes to risk stratification subgroups. L, low risk group; H, high risk group; TMB, tumor mutational burden.

and HuH-28) and in normal human intrahepatic biliary epithelial cells (HiBEpiCs). Compared with HiBEpiCs, *CD109* and *EFNB2* expression was significantly upregulated in HuCCT1 and RBE cells (P<0.001), and moderately upregulated in HuH-28 cells (P<0.01; Fig. 8A). Based on these results, HuCCT1 and RBE cells were selected for siRNA-mediated knockdown of *CD109* and *EFNB2*. Three siRNAs were designed for each gene, and their mRNA suppression efficiency was evaluated by RT-qPCR. In HuCCT1 cells, si-CD109-2 and si-EFNB2-3 showed the most significant downregulation (P<0.001; Fig. 8B), and were selected for subsequent experiments. After transfecting si-CD109 and si-EFNB2 into HuCCT1 and RBE cells, RT-qPCR confirmed significant reductions in *CD109* and *EFNB2* mRNA levels (P<0.001; Fig. 8C), indicating efficient transfection. WB further revealed significantly reduced CD109 and EFNB2 protein levels in both cell lines (P<0.001; Fig. 8D), consistent with mRNA changes.

*Functional assays for CD109 and EFNB2 knockdown in CCA cells*. To evaluate the effects of *CD109* and *EFNB2* knockdown on CCA cell behavior, cell proliferation was assessed using the CCK-8 assay at 0, 24, 48 and 72 h in HuCCT1 and RBE cells transfected with si-CD109, si-EFNB2 or si-NC (control). Compared with the si-NC group, knockdown of

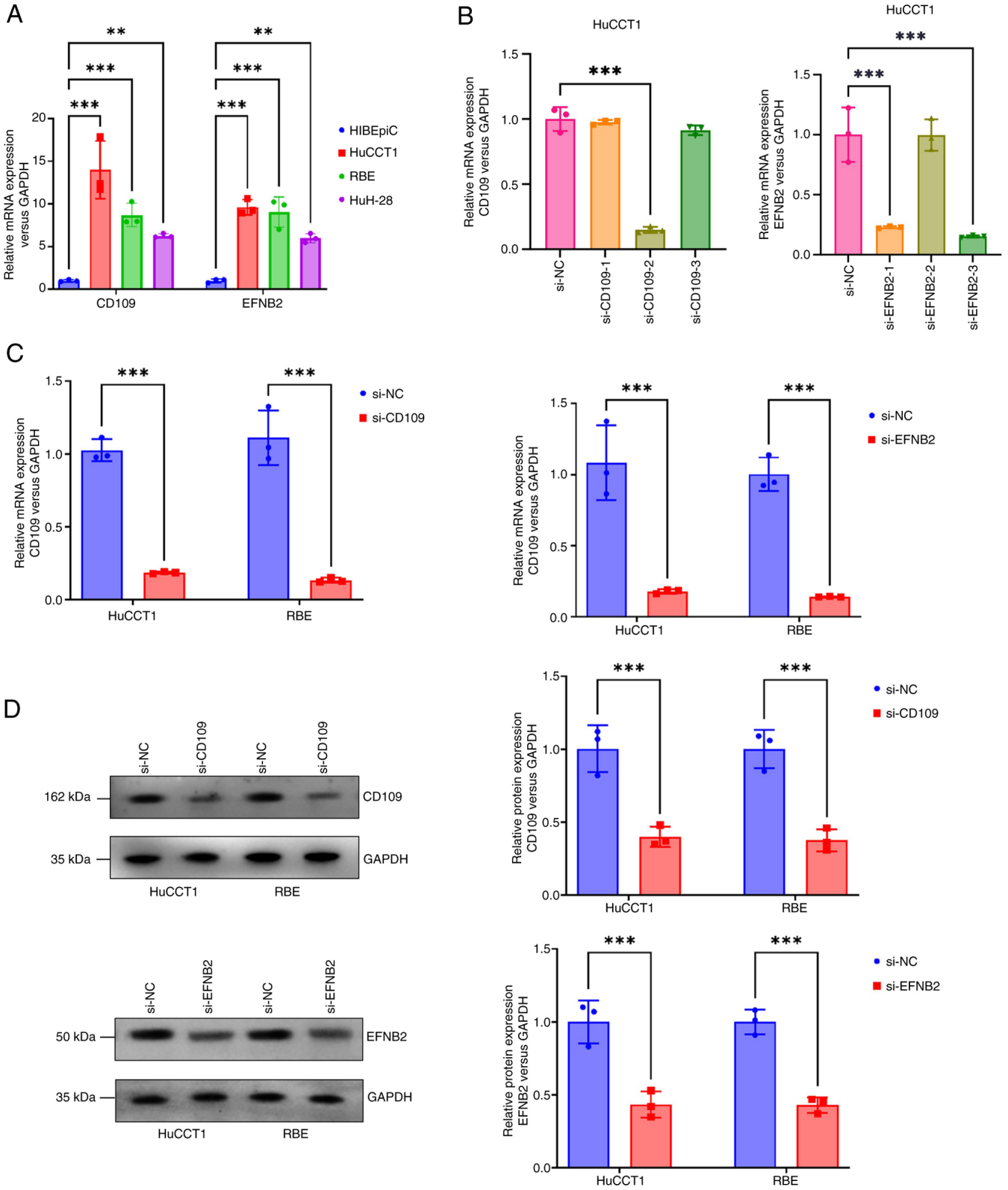


Figure 8. Establishment of CD109 and EFNB2 knockdown cholangiocarcinoma cell model. (A) mRNA expression levels of CD109 and EFNB2 in normal human intrahepatic biliary epithelial cells and CCA cell lines; (B) RT-qPCR validation of siRNA knockdown efficiency; (C) RT-qPCR validation of mRNA knockdown in HuCCT1 and RBE cells; (D) Western blotting validation of protein knockdown in HuCCT1 and RBE cells. $^{**}$P<0.01; $^{***}$P<0.001. si, small interfering; RT-qPCR, reverse transcription-quantitative PCR; NC, negative control.

*CD109* or *EFNB2* significantly reduced cell proliferation, with pronounced effects at 48 and 72 h (P<0.001); notably, si-CD109 exhibited stronger inhibition compared with si-EFNB2 (Fig. 9A). Clonogenic assays were performed to assess colony formation. HuCCT1 and RBE cells transfected with si-CD109 or si-EFNB2 formed significantly fewer colonies compared with the si-NC group (P<0.001; Fig. 9B). Wound healing assays evaluated cell migration. Compared with the si-NC

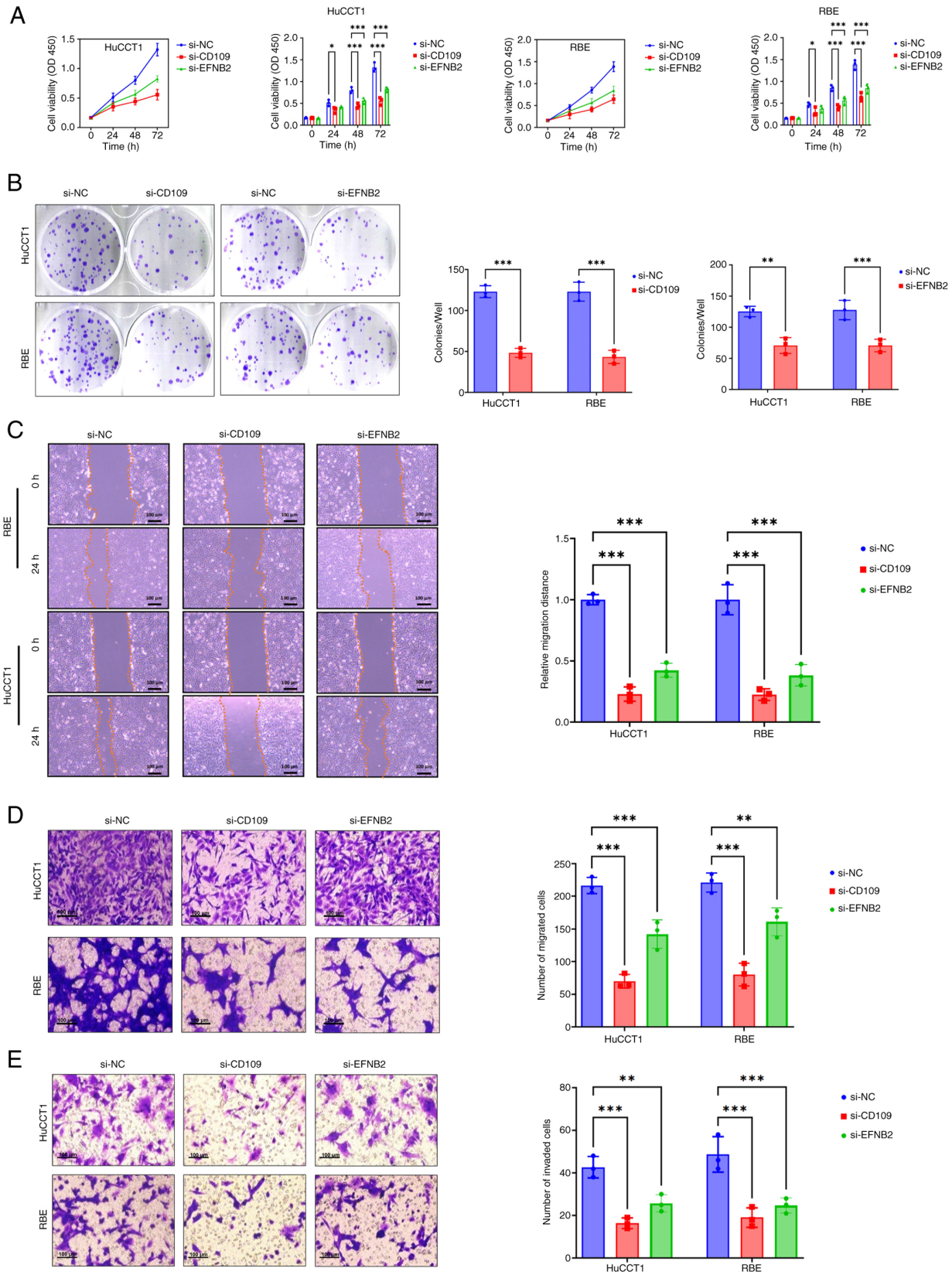


Figure 9. Functional assays following CD109 and EFNB2 knockdown in cholangiocarcinoma cells. (A) Cell Counting Kit-8 assay for cell proliferation; (B) clonogenic assay for colony formation; (C) wound healing assay for cell migration; (D) Transwell assay for cell migration; (E) Transwell assay for cell invasion. $^{*}$P<0.05, $^{**}$P<0.01, $^{***}$P<0.001. Scale bar, 100 $\mu$m. si, small interfering; NC, negative control.

group, the si-CD109 and si-EFNB2 groups exhibited significantly reduced wound closure in HuCCT1 and RBE cells, with si-CD109 showing greater inhibition (P<0.001; Fig. 9C). Transwell assays assessed migration and invasion. Migration assays showed significantly fewer migrating cells in si-CD109 and si-EFNB2 groups compared with si-NC (P<0.001;

Fig. 9D). Invasion assays revealed similarly reduced invasive cell numbers in both knockdown groups (P<0.001; Fig. 9E). These findings indicate that *CD109* and *EFNB2* knockdown significantly inhibits proliferation, colony formation, migration and invasion in HuCCT1 and RBE cells, suggesting their key roles in CCA progression.

*Role of EFNB2 and CD109 in disulfidptosis*. To investigate the role of EFNB2 and CD109 in disulfidptosis, immunofluorescence staining was carried out. The results (Fig. 10) showed that under glucose deprivation conditions, knocking down *EFNB2* or *CD109* in HuCCT1 and RBE cells induced cell shrinkage and abnormal F-actin aggregation. Treatment with the GLUT1 inhibitor BAY-876 exacerbated these morphological changes, with more pronounced actin depolymerization observed in the si-CD109 group, suggesting that CD109 may regulate cytoskeletal dynamics during disulfide bond accumulation. Intervention with the reducing agent TCEP largely alleviated F-actin aggregation in the si-CD109 group, but only partially in the si-EFNB2 group, indicating that EFNB2 may carry out a more key role in maintaining cytoskeletal stability. These findings suggest that the knockout of *EFNB2* and *CD109* enhances BAY-876-induced disulfidptosis, with TCEP preventing these effects.

## Discussion

In the present study, the first comprehensive analysis of disulfidptosis in CCA, a malignancy characterized by metabolic dysregulation and oxidative stress, was presented (1). By integrating transcriptomic profiling, molecular subtyping and prognostic modeling, its potential as a novel therapeutic target was unveiled. Through unsupervised clustering of 74 DRGs, two distinct molecular Subs (SubA and SubB) with significant differences in prognosis and the TME were identified. The more clinically aggressive SubB exhibited heightened disulfidptosis pathway activity. This finding mirrors observations in ferroptosis, where sublethal stress can foster tumor adaptation. It is hypothesized that under metabolic stress such as glucose deprivation CCA cells in the SubB adaptively leverage components of the disulfidptosis machinery, potentially through stress-activated pathways such as PI3K/AKT or MAPK/ERK (34-39), could enhance invasive potential.

Leveraging these Sub distinctions, a robust four-gene prognostic signature (*CD109, EFNB2, KLK6* and *ADAMTS12*) was developed and validated using LASSO Cox regression. This model effectively stratified patients into H- and L-risk groups, with the H-risk group showing significantly lower OS in both the training and validation cohorts. The strong predictive accuracy of the model for 1-, 2- and 3-year survival and its status as an independent prognostic factor highlight its clinical potential. The interplay between disulfidptosis and the TME is a key, yet underexplored, determinant of CCA progression. The findings of the present study reveal distinct immune profiles between the molecular Subs, with the aggressive SubB harboring an immunogenic yet profoundly immunosuppressive TME. CIBERSORT and ssGSEA analyses demonstrated that SubB, despite enhanced infiltration of effector immune cells such as $CD8^+$ T cells, also exhibited significant upregulation of immune checkpoint genes (*PD-L1, LAG3, CD47* and *TNFRSF9*) and HLA-related genes. This 'activated-exhausted' phenotype where cytotoxic lymphocytes co-express inhibitory checkpoint molecules, points toward a compromised antitumor response and aligns with the worse survival outcomes of the Sub (40-43).

GSEA provided a compelling mechanistic association for this phenotype, revealing a significant enrichment of the TGF-β signaling pathway in SubB. Mechanistically, it is hypothesized that sustained TGF-β signaling orchestrates this immunosuppressive landscape. While TGF-β can initially act as a chemoattractant for effector immune cells such as $CD8^+$ T cells, its chronic presence drives extensive extracellular matrix (ECM) remodeling and induces the expression of multiple immune checkpoints on both tumor and stromal cells (44,45). Within this remodeled TME, infiltrating $CD8^+$ T cells rapidly transition from an activated to an exhausted state, characterized by functional impairment and high inhibitory receptor expression. This 'activation-to-exhaustion' shift effectively aborts antitumor immunity and promotes malignant progression, suggesting that targeting the TGF-β axis could be key to reversing immunosuppression in these patients.

The prognostic signature of the present study is anchored by four genes: *CD109, EFNB2, KLK6* and *ADAMTS12*. Among these, *CD109* and *EFNB2* possess the highest risk coefficients and are intrinsically associated with this TGF-β driven malignancy. CD109 functions as a negative co-receptor for TGF-β, acting as a rheostat that suppresses canonical tumor-suppressive signals while enhancing pro-tumorigenic outputs such as EMT (46-48). EFNB2, through Ephrin receptor signaling, activates downstream pathways to promote the dynamic cytoskeletal remodeling essential for invasion and metastasis (49-51). *In vitro* validation confirmed their roles as key drivers of CCA malignancy. Silencing either *CD109* or *EFNB2* markedly suppressed proliferation, migration and invasion. Mechanistically, it was demonstrated that these genes protect CCA cells from glucose starvation-induced disulfidptosis, an effect that was reversed by the reducing agent TCEP. Immunofluorescence analysis revealed that silencing these genes led to F-actin cytoskeletal collapse under metabolic stress. It is therefore hypothesized that CD109 and EFNB2 confer resistance to disulfidptosis by preserving cytoskeletal integrity through redox modulation, possibly by enhancing NADPH regeneration or regulating SLC7A11-dependent cystine metabolism to maintain the glutathione pool (52). Concurrently, they might restrain the excessive actin network polymerization seen in disulfidptosis by influencing key regulatory nodes, such as the Rac1-WAVE pathway that governs actin dynamics. Future investigations employing metabolomics, live-cell redox imaging and non-reducing protein electrophoresis will be essential to systematically assess the way CD109 or EFNB2 depletion alters intracellular NADPH pools, thioredoxin system activity and actin disulfide cross-linking.

Beyond the experimentally validated markers, the prognostic signature of the present study incorporates *KLK6* and *ADAMTS12*. The inclusion of these genes is justified by robust bioinformatic and literature-based evidence. Both genes are significantly upregulated in CCA tumors and are associated with worse survival, aligning with their positive risk coefficients from LASSO regression. KLK6, a serine protease, exerts

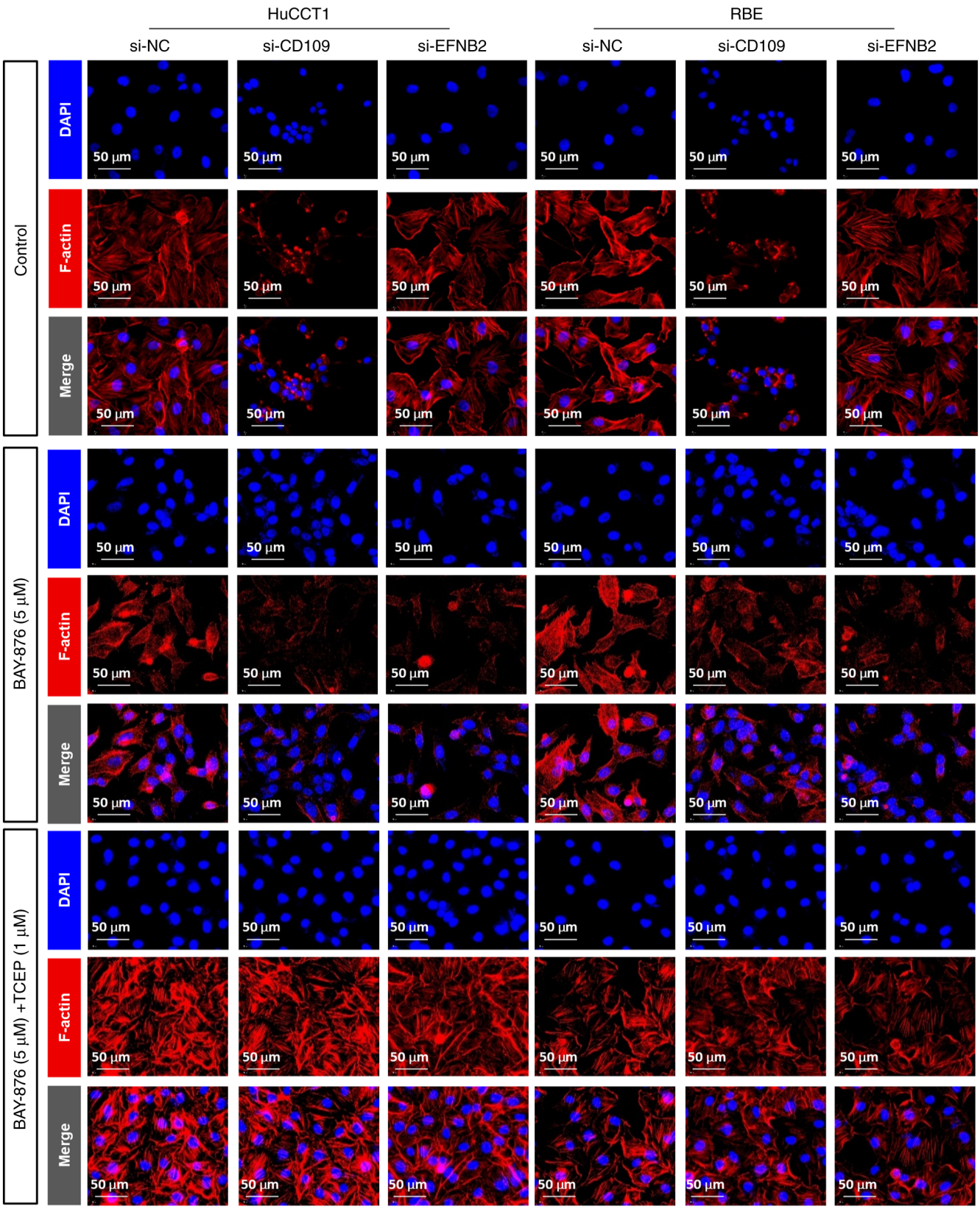


Figure 10. F-actin and nuclei in HuCCT1 and RBE cells transfected with si-NC, si-CD109 or si-EFNB2 and treated with 5 $\mu$M BAY-876 or 1 $\mu$M TCEP for 24 h. si, small interfering; NC, negative control; TCEP, Tris-(2-carboxyethyl)-phosphine hydrochloride.

dual roles in inflammation and tumor progression (53,54). In pancreatic ductal adenocarcinoma (PDAC), KLK6 promotes invasiveness, indicating potential therapeutic relevance for CCA (54). ADAMTS12, a metalloproteinase, modulates ECM remodeling in inflammation, fibrosis and cancer. In PDAC, ADAMTS12 enhances cell migration, while in hepatocellular carcinoma, it is associated with poor differentiation and recurrence (55,56). By collectively shaping a microenvironment

conducive to tumor invasion and metastasis, these two genes serve as rational and key components of the H-risk prognostic model of the present study. Elucidating their direct functional roles in the disulfidptosis pathway remains an important direction for future investigation.

Despite the novel insights provided by the present study, several limitations should be acknowledged. First, the reliance on public databases, particularly TCGA-CHOL cohort with its limited sample size (n=35), may constrain the statistical power and generalizability of the prognostic model and limits its utility for more detailed investigations, such as Sub analyses. A key limitation is that the TMB analysis was confined to TCGA cohort, as comprehensive mutation data were unavailable in other datasets, thereby precluding independent validation of these findings. Furthermore, the prognostic model is derived from bioinformatic approaches and awaits validation with prospective clinical data. Therefore, large-scale, multi-center prospective studies are essential to confirm its clinical robustness. Second, while the functional roles of *CD109* and *EFNB2* were established, the contributions of the other two signature genes *KLK6* and *ADAMTS12* to disulfidptosis and CCA progression remain to be experimentally elucidated, which is a direction for future research. Third, the drug sensitivity analysis was based solely on computational predictions, which may not fully capture the complexity of the TME. Experimental validation in clinically relevant models such as patient-derived organoids or xenografts is necessary to assess the therapeutic potential of the predicted agents. Finally, regarding clinical translation, although measuring the expression of signature genes such as *CD109* and *EFNB2* in patient samples for example via immunohistochemistry on FFPE tissues is technically feasible, establishing standardized and reproducible protocols is a key prerequisite for future clinical application.

In conclusion, the DRG risk model developed in the present study provides a valuable tool for survival prediction in patients with CCA, reinforcing the central role of disulfidptosis in CCA pathogenesis. Specifically, *CD109* and *EFNB2*, by collaboratively regulating cytoskeletal stability, metabolic reprogramming and immune suppression, hold promise as potential therapeutic targets for reversing tumor progression and overcoming treatment resistance. This not only offers important insights for personalized treatment strategies, but also lays the theoretical foundation for the development of disulfidptosis-based precision therapies in CCA.

## Acknowledgements

Not applicable.

## Funding

The present study was financially supported by the Changzhou Sci & Tech Program (grant no. CJ20220064, CJ20243007), the 2023 Changzhou Health Commission Science and Technology Project (grant no. QY202301), Youth Talent Science and Technology Project of Changzhou Health Commission (grant no. QN202434), Science and Technology Project of Changzhou Health Commission (grant no. ZD202428) and Top Talent of Changzhou 'The 14th Five-Year Plan' High-level Health Personnel Training Project (grant no. 2022260).

## Availability of data and materials

The data generated in the present study may be requested from the corresponding author.

## Authors' contributions

YC, JWu, DZha and WH contributed to the conception and design of the study. YC, WH, DZhu, LJ and JWa were involved in the acquisition, analysis and interpretation of the data. YC and WH drafted the manuscript. DZhu, LJ and JWa critically revised the manuscript for important intellectual content. JWu, DZha and WH supervised the study. YC and WH confirm the authenticity of all the raw data. All authors read and approved the final manuscript and agreed to take responsibility for all aspects of the work.

## Ethics approval and consent to participate

Not applicable.

## Patient consent for publication

Not applicable.

## Competing interests

The authors declare that they have no competing interests.

## References

1. Brindley PJ, Bachini M, Ilyas SI, Khan SA, Loukas A, Sirica AE, Teh BT, Wongkham S and Gores GJ: Cholangiocarcinoma. Nat Rev Dis Primers 7: 65, 2021.
2. Cardinale V: Classifications and misclassification in cholangiocarcinoma. Liver Int 39: 260-212, 2019.
3. Banales JM, Cardinale V, Carpino G, Marzioni M, Andersen JB, Invernizzi P, Lind GE, Folseraas T, Forbes SJ, Fouassier L, *et al*: Expert consensus document: Cholangiocarcinoma: Current knowledge and future perspectives consensus statement from the European network for the study of cholangiocarcinoma (ENS-CCA). Nat Rev Gastroenterol Hepatol 13: 261-280, 2016.
4. Clements O, Eliahoo J, Kim JU, Taylor-Robinson SD and Khan SA: Risk factors for intrahepatic and extrahepatic cholangiocarcinoma: A systematic review and meta-analysis. J Hepatol 72: 95-103, 2020.
5. Sirica AE, Gores GJ, Groopman JD, Selaru FM, Strazzabosco M, Wei Wang X and Zhu AX: Intrahepatic cholangiocarcinoma: Continuing challenges and translational advances. Hepatology 69: 1803-1815, 2019.
6. Fabris L, Perugorria MJ, Mertens J, Björkström NK, Cramer T, Lleo A, Solinas A, Sänger H, Lukacs-Kornek V, Moncsek A, *et al*: The tumour microenvironment and immune milieu of cholangiocarcinoma. Liver Int 39 (Suppl 1): S63-S78, 2019.
7. Arrivé L and Djelouah M: Refining prognosis in intrahepatic cholangiocarcinoma: The expanding role of imaging. Radiol Imaging Cancer 7: e250383, 2025.
8. PDQ Adult Treatment Editorial Board. Bile duct cancer (cholangiocarcinoma) treatment (PDQ®): Health Professional Version. In: PDQ Cancer Information Summaries. National Cancer Institute, Bethesda, MD, 2002.
9. Lockie EB, Sylivris A, Pandanaboyana S, Zalcberg J, Skandarajah A and Loveday BP: Relationship between pancreatic cancer resection rate and survival at population level: Systematic review. BJS Open 9: zraf007, 2025.
10. Valle JW, Lamarca A, Goyal L, Barriuso J and Zhu AX: New horizons for precision medicine in biliary tract cancers. Cancer Discov 7: 943-962, 2017.

11. Banales JM, Marin JJG, Lamarca A, Rodrigues PM, Khan SA, Roberts LR, Cardinale V, Carpino G, Andersen JB, Braconi C, *et al*: Cholangiocarcinoma 2020: The next horizon in mechanisms and management. Nat Rev Gastroenterol Hepatol 17: 557-588, 2020.
12. Kerr JF, Wyllie AH and Currie AR: Apoptosis: A basic biological phenomenon with wide-ranging implications in tissue kinetics. Br J Cancer 26: 239-257, 1972.
13. Tang D, Kang R, Berghe TV, Vandenabeele P and Kroemer G: The molecular machinery of regulated cell death. Cell Res 29: 347-364, 2019.
14. Shi Y, Wang Y, Niu K, Zhang W, Lv Q and Zhang Y: How CLSPN could demystify its prognostic value and potential molecular mechanism for hepatocellular carcinoma: A crosstalk study. Comput Biol Med 172: 108260, 2024.
15. Shi Y, Wang Y, Niu K and Zhang Y: A commentary on 'A bibliometric analysis of gastric cancer liver metastases: Advances in mechanisms of occurrence and treatment options'. Int J Surg 110: 5897-5898, 2024.
16. Liu X, Nie L, Zhang Y, Yan Y, Wang C, Colic M, Olszewski K, Horbath A, Chen X, Lei G, *et al*: Actin cytoskeleton vulnerability to disulfide stress mediates disulfidptosis. Nat Cell Biol 25: 404-414, 2023.
17. Liu X, Zhuang L and Gan B: Disulfidptosis: Disulfide stress-induced cell death. Trends Cell Biol 34: 327-337, 2024.
18. Zheng T, Liu Q, Xing F, Zeng C and Wang W: Disulfidptosis: A new form of programmed cell death. J Exp Clin Cancer Res 42: 137, 2023.
19. Tang J, Peng X, Xiao D, Liu S, Tao Y and Shu L: Disulfidptosis-related signature predicts prognosis and characterizes the immune microenvironment in hepatocellular carcinoma. Cancer Cell Int 24: 19, 2024.
20. Zhang HB, Pan JY and Zhu T: A disulfidptosis-related lncRNA prognostic model to predict survival and response to immunotherapy in lung adenocarcinoma. Front Pharmacol 14: 1254119, 2023.
21. Huang J, Zhang J, Zhang F, Lu S, Guo S, Shi R, Zhai Y, Gao Y, Tao X, Jin Z, *et al*: Identification of a disulfidptosis-related genes signature for prognostic implication in lung adenocarcinoma. Comput Biol Med 165: 10740. 2023.
22. Chen Y, Xue W, Zhang Y, Gao Y and Wang Y: A novel disulfidptosis-related immune checkpoint genes signature: Forecasting the prognosis of hepatocellular carcinoma. J Cancer Res Clin Oncol 149: 12843-12854, 2023.
23. Dong X, Liao P, Liu X, Yang Z, Wang Y, Zhong W and Wang B: Construction and validation of a reliable disulfidptosis-related LncRNAs signature of the subtype, prognostic, and immune landscape in colon cancer. Int J Mol Sci 24: 12915, 2023.
24. Kang K, Li X, Peng Y and Zhou Y: Comprehensive analysis of disulfidptosis-related LncRNAs in molecular classification, immune microenvironment characterization and prognosis of gastric cancer. Biomedicines 11: 3165, 2023.
25. Feng Z, Zhao Q, Ding Y, Xu Y, Sun X, Chen Q, Zhang Y, Miao J and Zhu J: Identification a unique disulfidptosis classification regarding prognosis and immune landscapes in thyroid carcinoma and providing therapeutic strategies. J Cancer Res Clin Oncol 149: 11157-11170, 2023.
26. Qi C, Ma J, Sun J, Wu X and Ding J: The role of molecular subtypes and immune infiltration characteristics based on disulfidptosis-associated genes in lung adenocarcinoma. Aging (Albany NY) 15: 5075-5095, 2023.
27. Raggi C, Taddei ML, Rae C, Braconi C and Marra F: Metabolic reprogramming in cholangiocarcinoma. J Hepatol 77: 849-864, 2022.
28. Duwe L, Fouassier L, Lafuente-Barquero J and Andersen JB: Unraveling the actin cytoskeleton in the malignant transformation of cholangiocyte biology. Transl Oncol 26: 101531, 2022.
29. Zhao X, Zhang M, He J, Li X and Zhuang X: Emerging insights into ferroptosis in cholangiocarcinoma (review). Oncol Lett 28: 606, 2024.
30. R Core Team. R: A language and environment for statistical computing. R Foundation for Statistical Computing, Vienna, 2024. URL https://www.R-project.org/.
31. Mayakonda A, Lin DC, Assenov Y, Plass C and Koeffler HP: Maftools: Efficient and comprehensive analysis of somatic variants in cancer. Genome Res 28: 1747-1756, 2018.
32. Wilkerson MD and Hayes DN: ConsensusClusterPlus: A class discovery tool with confidence assessments and item tracking. Bioinformatics 26: 1572-1573, 2010.
33. Livak KJ and Schmittgen TD: Analysis of relative gene expression data using real-time quantitative PCR and the 2(-Delta Delta C(T)) method. Methods 25: 402-408, 2001.
34. Jiang X, Stockwell BR and Conrad M: Ferroptosis: Mechanisms, biology and role in disease. Nat Rev Mol Cell Biol 22: 266-282, 2021.
35. Zhang ZJ, Huang YP, Li XX, Liu ZT, Liu K, Deng XF, Xiong L, Zou H and Wen Y: A novel ferroptosis-related 4-gene prognostic signature for cholangiocarcinoma and photodynamic therapy. Front Oncol 11: 747445, 2021.
36. Amontailak S, Titapun A, Jusakul A, Thanan R, Kimawaha P, Jamnongkan W, Thanee M, Sirithawat P and Techasen A: Prognostic values of ferroptosis-related proteins ACSL4, SLC7A11, and CHAC1 in cholangiocarcinoma. Biomedicines 12: 2091, 2024.
37. Wan S, Liang C, Wu C, Wang S, Wang J, Xu L, Zhang X, Hou Y, Xia Y, Xu L and Huang X: Disulfidptosis in tumor progression. Cell Death Discov 11: 205, 2025.
38. Hu F and Lito P: Insights into how adeno-squamous transition drives KRAS inhibitor resistance. Cancer Cell 42: 330-332, 2024.
39. Mi T, Kong X, Chen M, Guo P and He D: Inducing disulfidptosis in tumors: Potential pathways and significance. MedComm (2020) 5: e791, 2024.
40. Xiao Y, Li ZZ, Zhong NN, Cao LM, Liu B and Bu LL: Charting new frontiers: Co-inhibitory immune checkpoint proteins in therapeutics, biomarkers, and drug delivery systems in cancer care. Transl Oncol 38: 101794, 2023.
41. Cruz D, Rodríguez-Romanos R, González-Bartulos M, García-Cadenas I, de la Cámara R, Heras I, Buño I, Santos N, Lloveras N, Velarde P, *et al*: LAG3 genotype of the donor and clinical outcome after allogeneic transplantation from HLA-identical sibling donors. Front Immunol 14: 1066393, 2023.
42. Perea F, Sánchez-Palencia A, Gómez-Morales M, Bernal M, Concha Á, García MM, González-Ramírez AR, Kerick M, Martin J, Garrido F, *et al*: HLA class I loss and PD-L1 expression in lung cancer: Impact on T-cell infiltration and immune escape. Oncotarget 9: 4120-4133, 2017.
43. Saigí M, Mate JL, Carcereny E, Martínez-Cardús A, Esteve A, Andreo F, Centeno C, Cucurull M, Mesia R, Pros E and Sanchez-Cespedes M: HLA-I levels correlate with survival outcomes in response to immune checkpoint inhibitors in non-small cell lung cancer. Lung Cancer 189: 107502, 2024.
44. Itatani Y, Kawada K and Sakai Y: Transforming growth Factor-β signaling pathway in colorectal cancer and its tumor microenvironment. Int J Mol Sci 20: 5822, 2019.
45. Hao Y, Baker D and Ten Dijke P: TGF-β-mediated epithelial-mesenchymal transition and cancer metastasis. Int J Mol Sci 20: 2767, 2019.
46. Naoi H, Suzuki Y, Miyagi A, Horiguchi R, Aono Y, Inoue Y, Yasui H, Hozumi H, Karayama M, Furuhashi K, *et al*: CD109 attenuates bleomycin-induced pulmonary fibrosis by inhibiting TGF-β signaling. J Immunol 212: 1221-1231, 2024.
47. Taki T, Shiraki Y, Enomoto A, Weng L, Chen C, Asai N, Murakumo Y, Yokoi K, Takahashi M and Mii S: CD109 regulates in vivo tumor invasion in lung adenocarcinoma through TGF-β signaling. Cancer Sci 111: 4616-4628, 2020.
48. Litvinov IV, Bizet AA, Binamer Y, Jones DA, Sasseville D and Philip A: CD109 release from the cell surface in human keratinocytes regulates TGF-β receptor expression, TGF-β signalling and STAT3 activation: Relevance to psoriasis. Exp Dermatol 20: 627-632, 2011.
49. Zeng X, Hunt A, Jin SC, Duran D, Gaillard J and Kahle KT: EphrinB2-EphB4-RASA1 signaling in human cerebrovascular development and disease. Trends Mol Med 25: 265-286, 2019.
50. Zhu F, Dai SN, Xu DL, Hou CQ, Liu TT, Chen QY, Wu JL and Miao Y: EFNB2 facilitates cell proliferation, migration, and invasion in pancreatic ductal adenocarcinoma via the p53/p21 pathway and EMT. Biomed Pharmacother 125: 109972, 2020.
51. Xu C, Gu L, Kuerbanjiang M, Jiang C, Hu L, Liu Y, Xue H, Li J, Zhang Z and Xu Q: Adaptive activation of EFNB2/EPHB4 axis promotes post-metastatic growth of colorectal cancer liver metastases by LDLR-mediated cholesterol uptake. Oncogene 42: 99-112, 2023.
52. Koppula P, Zhang Y, Zhuang L and Gan B: Amino acid transporter SLC7A11/xCT at the crossroads of regulating redox homeostasis and nutrient dependency of cancer. Cancer Commun (Lond) 38: 12, 2018.

53. Hwang YS, Cho HJ, Park ES, Lim J, Yoon HR, Kim JT, Yoon SR, Jung H, Choe YK, Kim YH, *et al*: KLK6/PAR1 axis promotes tumor growth and metastasis by regulating cross-talk between tumor cells and macrophages. Cells 11: 4101, 2022.
54. Zhang L, Lovell S, De Vita E, Jagtap PKA, Lucy D, Goya Grocin A, Kjær S, Borg A, Hennig J, Miller AK and Tate EW: A KLK6 activity-based probe reveals a role for KLK6 activity in pancreatic cancer cell invasion. J Am Chem Soc 144: 22493-22504, 2022.
55. He RZ, Zheng JH, Yao HF, Xu DP, Yang MW, Liu DJ, Sun YW and Huo YM: ADAMTS12 promotes migration and epithelial-mesenchymal transition and predicts poor prognosis for pancreatic cancer. Hepatobiliary Pancreat Dis Int 22: 169-178, 2023.
56. Dekky B, Azar F, Bonnier D, Monseur C, Kalebić C, Arpigny E, Colige A, Legagneux V and Théret N: ADAMTS12 is a stromal modulator in chronic liver disease. FASEB J 37: e23237, 2023.